A Semi-Spectral Numerical Method for Modeling the Vorticity Dynamics of the near-Core region of Hurricane-Like Vortices

By
Michael T. Montgomery, Juan Marcus Hidalgo and Paul Reasor

Department of Atmospheric Science
Colorado State University
Fort Collins, Colorado

Research supported by the Office of Naval Research, #N00014-93-1-0456 MOD P00007

Colorado State University

Department of Atmospheric Science

Paper No. 695

A SEMI-SPECTRAL NUMERICAL METHOD FOR MODELING THE VORTICITY DYNAMICS OF THE NEAR-CORE REGION OF HURRICANE-LIKE VORTICES

Michael T. Montgomery, Juan Marcus Hidalgo, and Paul D. Reasor

Research supported through the Civilian Institute Program of the Air Force Institute of Technology (AFIT) and by ONR N00014-93-1-0456 P0006

Principal Investigator: Michael T. Montgomery

Department of Atmospheric Science

Colorado State University

Fort Collins, CO 80523

July 2000

Atmospheric Science Paper No. 695

ABSTRACT

In recent years, numerical weather prediction models have progressed from finite difference methods to spectral methods in order to obtain more accurate forecasts in less computational time. A switch from "pure" finite difference to "pure" spectral techniques, however, may not be the best approach in all cases. Indeed, for some problems a mixed approach with finite difference approximations in one coordinate and spectral approximations in the remaining coordinates may provide comparably accurate results in less computational time than either pure method alone. This is particularly evident for the case of a hurricane where a state of near-circular symmetry typically prevails. For such a problem, a semi-spectral (SS) method using finite difference approximations in the radial direction and spectral methods in the azimuthal direction is a natural choice.

While the effectiveness of pure methods for certain problems in fluid dynamics and atmospheric dynamics is well documented, comparatively little work has been undertaken to examine the effectiveness of SS schemes. This is particularly evident in problems concerning the vorticity dynamics of the hurricane near-core region. Because of the nearly circular flow of a strong hurricane, we hypothesize that SS formulations may prove useful in helping to elucidate the asymmetric vorticity dynamics in the hurricane's near-core region. This study examines the effectiveness of the semi-spectral approach for two classes of problems. The first problem concerns the redistribution of vorticity anomalies within a "master" vortex possessing a vorticity profile which decreases monotonically with radius. The second problem concerns barotropic instability, vortex breakdown, and vorticity mixing that is observed in mature hurricanes.

For simplicity, we confine our attention to barotropic nondivergent dynamics on an f-plane. The particular SS model used is an extension of the linear model of Montgomery

and Kallenbach (1997) to include the nonlinear advective terms. We compare the results of this model against finite difference (FD) and spectral (SP) model predictions.

In the first set of experiments, predictions of the SS model were virtually identical to those of the SP and FD models on all scales including the evolution of the vorticity field, changes in the mean profiles, and structure and intensity of the endstate. Additionally, the SS model produced these results in significantly less computer time than both the SP and FD models for the numerical parameters chosen. In the second set of experiments, the SS model performed nearly as well in simulating barotropic instability and vorticity mixing in a mature hurricane-like vortex modeled as an annular ring of elevated vorticity. The results obtained in this case are a bit more realistic than the results of Schubert, et al. (1999) in which a similar but larger vortex was examined. In our case, the elevated value of vorticity was higher, and the corresponding growth rates were stronger. This resulted in a 14 h mixing period with a pressure drop of 12 mb as compared to a 36 h mixing period and an 8 mb pressure drop observed in the Schubert, et al. simulation. Our simulated mixing time is believed a more realistic estimate of the mixing timescale for mature hurricanes. As with the first experiment, the SS model achieved these results in less computer time than the SP model for the numerical parameters chosen.

Based on these results and other analyses, we then assess the strengths and weaknesses of the SS approach in simulating diverse aspects of hurricane near-core vorticity dynamics.

ACKNOWLEDGEMENTS

This work was supported through the Civilian Institute Program of the Air Force Institute of Technology (AFIT) and by ONR N00014-93-1-0456 P0006. Numerical computations were performed using Hewlett Packard (HP) Apollo series computers belonging to the Montgomery Research Project. Programs were written in HP FORTRAN 9000 and in the Interactive Data Language (IDL) of Research Systems, Inc.

Chapter 1

INTRODUCTION

In 1950 Charney, Fjørtoft, and von Neumann produced the first successful numerical weather forecast of the nondivergent barotropic vorticity equation using meteorological data. Their achievement ushered in a new era in atmospheric science which relies heavily on computers. Since then, a significant portion of atmospheric research has focused on the exploitation of computer resources to better understand and more accurately predict atmospheric motions. This is especially true in the field of hurricane research where forecast errors can be costly. Researchers are constantly striving to develop models that produce better forecasts while using the least amount of computer time. In this effort, they have the choice of employing either finite difference methods or spectral methods to approximate the differential equations governing atmospheric motions.

What if one were to incorporate both methods into a single model and take advantage of the simplicity of finite difference approximations and the near-exactness of spectral methods? Could this produce a better model which is faster with comparable accuracy? Would it be a useful tool for hurricane research? The answers to these questions and others are the subjects of this thesis. The focus of our study is an examination of a "hybrid" numerical model that incorporates finite difference and spectral methods into a single model of the hurricane near-core region. We assess the effectiveness of this scheme in simulating near-core vortex dynamics as compared to "pure" schemes for two classes of vortices, a tropical depression-like vortex and a mature hurricane-like vortex.

For simplicity, we restrict our focus to the barotropic nondivergent vorticity dynamics on an f-plane. The two "pure" models, which are the controls for our study, are a finite difference and a spectral model that represent the vorticity evolution on a Cartesian grid

and use finite differences and spectral transforms in each coordinate, respectively. Our "hybrid" model, which will be referred to as the "semispectral" (SS) model, is formulated on a cylindrical coordinate grid and employs finite difference approximations in the radial coordinate and spectral transforms in the azimuthal coordinate. It is an extension of the linear model that Montgomery and Kallenbach (1997– henceforth MK) used in their study of hurricane spiral bands and intensity changes, to include nonlinear advective terms. Part of the reason we expect this scheme to be beneficial in modeling hurricane-like vortices is because we are taking advantage of the near-cylindrical symmetry of observed hurricane flow.

A similar approach was adopted for a barotropic fluid with a free surface by Willoughby (1988, 1992, 1990, 1994, 1995) and by Montgomery, Möeller, and Nicklas (1999) in their studies of hurricane motion on a β plane. In these works, the focus was on the dynamics of hurricane motion and not on the numerics, per se. In this thesis, we place equal emphasis on determining the performance characteristics of the SS model and in obtaining new insight into the vortex dynamics of the near-core region of tropical cyclone-like vortices. To determine how our SS technique performs relative to other numerical methods, we compare the SS model to a finite difference (FD) model and a spectral (SP) model.

An outline of this thesis is as follows. We begin with a summary of the three models utilized for our comparisons. We next point out the basic differences between the models and explain how each is initialized. We then motivate and describe the experiments that are to be performed and present the main results for each experiment. Finally, we assess how the SS model performs as compared to the FD and SP models.

Chapter 2

DESCRIPTION OF MODELS

2.1 Introduction

This chapter describes the numerical models used in our study. Beginning with the governing equation of motion, the essential characteristics of each model are summarized including the model domains, numerical methods employed to compute spatial derivatives, time-stepping algorithm, boundary conditions and others.

2.2 Governing Equation

The governing equation is the vorticity equation for two-dimensional nondivergent barotropic flow. The vorticity equation is derived from the two-dimensional barotropic nondivergent momentum and continuity equations for a Navier-Stokes fluid on an f-plane:

$$\frac{\partial u}{\partial t} + u\frac{\partial u}{\partial x} + v\frac{\partial u}{\partial y} - fv + \frac{1}{\rho}\frac{\partial p}{\partial x} = \nu\nabla^2 u \tag{2.1}$$

$$\frac{\partial v}{\partial t} + u\frac{\partial v}{\partial x} + v\frac{\partial v}{\partial y} + fu + \frac{1}{\rho}\frac{\partial p}{\partial y} = \nu\nabla^2 v \tag{2.2}$$

$$\frac{\partial u}{\partial x} + \frac{\partial v}{\partial y} = 0 \tag{2.3}$$

where u and v are the eastward and northward components of velocity, respectively, f is the constant Coriolis parameter, ρ is the constant density, p is the pressure, ν is the constant kinematic viscosity, and $\nabla^2 = \partial^2/\partial x^2 + \partial^2/\partial y^2$ is the Laplacian operator. Cross differentiating the momentum equations eliminates the pressure gradient from the dynamics. Using the continuity equation yields the vertical vorticity equation:

$$\frac{\partial \zeta}{\partial t} + u\frac{\partial \zeta}{\partial x} + v\frac{\partial \zeta}{\partial y} = \nu \nabla^2 \zeta, \tag{2.4}$$

where $\zeta = \partial v/\partial x - \partial u/\partial y$. Defining a streamfunction ψ such that $u = -\partial\psi/\partial y$ and $v = \partial\psi/\partial x$ ensures that (2.3) is satisfied. The vorticity is related to the streamfunction via a Poisson equation:

$$\nabla^2 \psi = \zeta, \tag{2.5}$$

referred to colloquially as the *invertibility principle*. Given ζ one can deduce the winds by solving (2.5) for the streamfunction:

$$\psi = \nabla^{-2} \zeta, \tag{2.6}$$

where ∇^{-2} is the inverse of the Laplacian. Using our definition of the streamfunction, (2.4) becomes:

$$\frac{\partial \zeta}{\partial t} - \frac{\partial \psi}{\partial y}\frac{\partial \zeta}{\partial x} + \frac{\partial \psi}{\partial x}\frac{\partial \zeta}{\partial y} = \nu \nabla^2 \zeta, \tag{2.7}$$

or

$$\frac{\partial \zeta}{\partial t} + \frac{\partial(\psi, \zeta)}{\partial(x, y)} = \nu \nabla^2 \zeta, \tag{2.8}$$

where $\partial(\psi,\zeta)/\partial(x,y) = (\partial\psi/\partial x)(\partial\zeta/\partial y) - (\partial\psi/\partial y)(\partial\zeta/\partial x)$ is the Jacobian of ψ and ζ with respect to x and y. Eq. (2.8) may be written equivalently as:

$$\frac{D}{Dt}\zeta = \nu \nabla^2 \zeta, \tag{2.9}$$

where

$$\frac{D}{Dt} = \frac{\partial}{\partial t} + u\frac{\partial}{\partial x} + v\frac{\partial}{\partial y} = \frac{\partial}{\partial t} - \frac{\partial \psi}{\partial y}\frac{\partial}{\partial x} + \frac{\partial \psi}{\partial x}\frac{\partial}{\partial y}. \tag{2.10}$$

Eq. (2.9) states that the material rate of change of vorticity is altered by horizontal diffusion of vorticity.

2.3 Model Domains

The SS model is formulated in cylindrical coordinates while the SP and FD models are formulated in Cartesian coordinates. As a result, the domain of the SS model is chosen to be a circle whose diameter is equal to the length of the longest diagonal in the two Cartesian models. For all results presented here, the domains of the SP and FD models are assumed to be square, and the SS domain is the circle that circumscribes this square (see Fig. 2.1). This ensures that the longest distance represented in the SP and FD models is also the longest distance represented in the SS model.

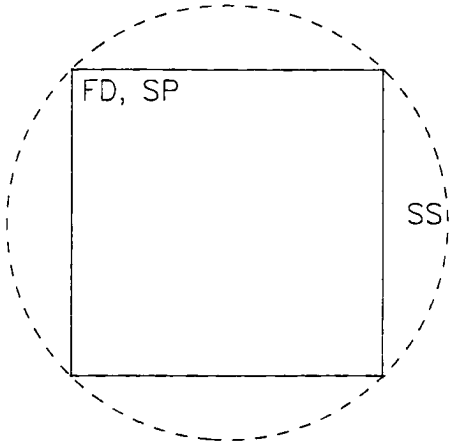

Figure 2.1: Schematic showing the relationship between the domain shapes of the models. The solid line indicates the shape of the outer boundary of the SP and FD models, while the dashed line shows the shape of the outer boundary of the SS model. The domain of the SS model is the circle that circumscribes the square domain of the SP and FD models.

2.4 Common Model Features

2.4.1 Time-Stepping Algorithm

All three models in this study employ a fourth order Runge Kutta time-stepping algorithm as described in Haltiner and Williams (1980).

2.4.2 Initialization

All models are initialized with a field of vorticity expressed as the sum of basic state (or azimuthal mean) and perturbation components. Derived quantities such as streamfunction and/or winds based on this initial condition are obtained by solving the invertibility relation (Eq. (2.6)).

2.4.3 Vorticity Corrections

For the FD and SP models, the doubly periodic nature of their domains (see Sections 2.5 and 2.6) requires that the initial vorticity have zero net circulation. The initial vorticity is consequently corrected by first computing the correction factor $C = -\frac{1}{A}\int \zeta \, dA$ (where A is the area of the domain) and then adjusting the vorticity by $\zeta(\text{corrected}) = \zeta(\text{uncorrected}) + C$.

Since it is based on a cylindrical polar grid, the SS model does not need such a correction. However, to maintain consistency among the models, the initial vorticity field for the SS model is also corrected for zero net circulation.

2.4.4 Diffusion

Diffusion in all three models is accomplished via ∇^2 diffusion with a viscosity coefficient of $\nu = 100$ m^{2}s^{-1}. This value was chosen to be consistent with the experiments performed by Schubert et al. (1999; hereafter S99) in their study of polygonal eyewall dynamics and vorticity mixing processes for a mature hurricane-type vortex modeled as an annular region of elevated vorticity.

2.5 The Spectral Model

The first of our controls is the fully SP model used by S99. This particular model utilizes Fourier modes in both x and y on a doubly periodic Cartesian domain. The number of resolved modes is determined by the number of gridpoints in each direction. For example, if $2M$ gridpoints are used in x and $2N$ gridpoints are used in y, the model will resolve M and N modes in x and y, respectively. However, the user must specify the number of resolved modes to be kept in each direction to ensure fully dealiased calculations

of the quadratic advective terms in (2.7). In general, this requires at least $\frac{2}{3}M$ and $\frac{2}{3}N$ modes to be kept in x and y, respectively.

2.5.1 Accuracy of Spatial Derivatives

In the SP model, Fourier methods are used to represent the streamfunction and vorticity:

$$\zeta(x,y,t) = \sum_{\substack{|n|\leq N \\ |m|\leq M}} \hat{\zeta}_{m,n}(t) e^{i(mx+ny)}, \tag{2.11}$$

and

$$\psi(x,y,t) = \sum_{\substack{|n|\leq N \\ |m|\leq M}} \hat{\psi}_{m,n}(t) e^{i(mx+ny)}, \tag{2.12}$$

where $\hat{\zeta}_{m,n}$ is the vorticity amplitude, $\hat{\psi}_{m,n}$ is the streamfunction amplitude, n is the wavenumber in x, m is the wavenumber in y, N is the truncation in x, and M is the truncation in y. For a given truncation, the derivatives of the streamfunction and vorticity are computed exactly. As an illustration, consider the derivative of ζ with respect to x:

$$\frac{\partial \zeta}{\partial x} = \sum_{\substack{|n|\leq N \\ |m|\leq M}} im\hat{\zeta}_{m,n}(t) e^{i(mx+ny)}. \tag{2.13}$$

The invertibility principle (2.5) is also solved exactly:

$$\sum_{\substack{|n|\leq N \\ |m|\leq M}} -(m^2+n^2)\hat{\psi}_{m,n}(t) e^{i(mx+ny)} = \sum_{\substack{|n|\leq N \\ |m|\leq M}} \hat{\zeta}_{m,n}(t) e^{i(mx+ny)}, \tag{2.14}$$

or, for a given m and n (not both zero),

$$\hat{\psi}_{m,n}(t) = -\frac{1}{(m^2+n^2)}\hat{\zeta}_{m,n}(t). \tag{2.15}$$

2.5.2 Boundary Conditions

Since the SP model is formulated on a doubly periodic domain, the "boundary conditions" are simply periodicity in x and y.

2.5.3 Linearity

The SP model performs fully non-linear calculations and, due to its geometry, does not admit a simple linearization for a circular basic state vortex.

2.6 Finite Difference Model

The second control model is an FD model developed specifically for this study. It uses finite difference approximations in both x and y and assumes a doubly periodic Cartesian domain.

2.6.1 Accuracy of Spatial Derivatives

Spatial derivatives in the FD model are specified to be second order accurate. As such, the Jacobian is computed via Arakawa's (1966) second order advection scheme.

To invert the vorticity for the streamfunction (Eq. (2.6)), a fast elliptic solver developed by Paul Swarztrauber and Roland Sweet of the National Center for Atmospheric Research is employed. This solver is available on the internet at *http*: *www.netlib.org**toms*\541. See Swarztrauber and Sweet (1975), Chap. I., for documentation on this routine.

2.6.2 Boundary Conditions

Since the FD model is formulated on a doubly periodic domain, the "boundary conditions" are simply periodicity in x and y.

2.6.3 Linearity

The FD model performs fully non-linear calculations and, due to its geometry, does not admit a simple linearization for a circular basic state vortex.

2.7 The Semi-Spectral Model

The SS model is a simple extension of MK to include the nonlinear advective terms in the vorticity equation. Although the model was first summarized in Appendix B of Montgomery and Enagonio (1998–hereafter ME), the details of its derivation are presented here for completeness.

The model domain is chosen such that it circumscribes the square domains of the FD and SP models (see Fig. 2.1). The governing equation is subsequently based on the polar representation of Eq. (2.7):

$$\frac{\partial \zeta}{\partial t} - \frac{1}{r}\frac{\partial \psi}{\partial \lambda}\frac{\partial \zeta}{\partial r} + \frac{1}{r}\frac{\partial \psi}{\partial r}\frac{\partial \zeta}{\partial \lambda} = \nu \nabla^2 \zeta. \tag{2.16}$$

Writing the streamfunction (ψ) and vorticity (ζ) as sums of perturbation components ($\zeta'(r,\lambda,t)$ and $\psi'(r,\lambda,t)$) and azimuthal means ($\overline{\zeta}(r,t)$ and $\overline{\psi}(r,t)$), which do not depend on λ, we obtain the following tendency equation for the perturbation vorticity:

$$\frac{\partial \zeta'}{\partial t} = \frac{1}{r}\frac{\partial \psi'}{\partial \lambda}\frac{\partial \zeta'}{\partial r} - \frac{1}{r}\frac{\partial \psi'}{\partial r}\frac{\partial \zeta'}{\partial \lambda} + \frac{1}{r}\frac{\partial \psi'}{\partial \lambda}\frac{\partial \overline{\zeta}}{\partial r} - \frac{1}{r}\frac{\partial \overline{\psi}}{\partial r}\frac{\partial \zeta'}{\partial \lambda} + \nu \nabla^2 \zeta', \tag{2.17}$$

where the terms involving the azimuthal derivatives of the mean vorticity and mean streamfunction vanish by construction. We next convert (2.17) from *advective* to *flux form* by noting that:

$$\frac{1}{r}\frac{\partial \psi'}{\partial \lambda}\frac{\partial \zeta'}{\partial r} = \frac{1}{r}\frac{\partial}{\partial r}\Big(\zeta'\frac{\partial \psi'}{\partial \lambda}\Big) - \frac{\zeta'}{r}\frac{\partial^2 \psi'}{\partial r \partial \lambda} \tag{2.18}$$

and

$$-\frac{1}{r}\frac{\partial \psi'}{\partial r}\frac{\partial \zeta'}{\partial \lambda} = -\frac{1}{r}\frac{\partial}{\partial \lambda}\Big(\zeta'\frac{\partial \psi'}{\partial r}\Big) + \frac{\zeta'}{r}\frac{\partial^2 \psi'}{\partial r \partial \lambda}. \tag{2.19}$$

Substituting (2.18) and (2.19) into (2.17) yields our tendency equation in flux form:

$$\frac{\partial \zeta'}{\partial t} = \frac{1}{r}\Big[\frac{\partial}{\partial r}\Big(\zeta'\frac{\partial \psi'}{\partial \lambda}\Big) - \frac{\partial}{\partial \lambda}\Big(\zeta'\frac{\partial \psi'}{\partial r}\Big) + \frac{\partial \psi'}{\partial \lambda}\frac{\partial \overline{\zeta}}{\partial r} - \frac{\partial \overline{\psi}}{\partial r}\frac{\partial \zeta'}{\partial \lambda}\Big] + \nu \nabla^2 \zeta'. \tag{2.20}$$

The first two terms on the right hand side of Eq. (2.20) represent the nonlinear advection of perturbation vorticity by perturbation winds. The next two are both linear terms representing the advection of *mean* vorticity by *perturbation* winds and *perturbation* vorticity by *mean* winds, respectively. The last term is the diffusion term.

Since $\zeta' = \nabla^2 \psi'$ we may rewrite (2.20) as:

$$\nabla^2\Big(\frac{\partial \psi'}{\partial t}\Big) = \frac{1}{r}\Big[\frac{\partial}{\partial r}\Big(\zeta'\frac{\partial \psi'}{\partial \lambda}\Big) - \frac{\partial}{\partial \lambda}\Big(\zeta'\frac{\partial \psi'}{\partial r}\Big) + \frac{\partial \psi'}{\partial \lambda}\frac{\partial \overline{\zeta}}{\partial r} - \frac{\partial \overline{\psi}}{\partial r}\frac{\partial \zeta'}{\partial \lambda}\Big] + \nu \nabla^2 \zeta'. \tag{2.21}$$

In the SS method, we use Fourier modes to compute the azimuthal derivatives and finite difference approximations to compute the radial derivatives. The perturbation vorticity and streamfunction are therefore represented semi-spectrally. Suppressing the subscript notation for the discrete radial points, we write:

$$\psi'(r,\lambda,t) = \sum_{|l|\leq N} \hat{\psi}_l(r,t)e^{il\lambda}, \tag{2.22}$$

and

$$\zeta'(r,\lambda,t) = \sum_{|m|\leq N} \hat{\zeta}_m(r,t)e^{im\lambda}, \tag{2.23}$$

where $\hat{\psi}_l$ and $\hat{\zeta}_m$ are the Fourier amplitudes for the perturbation streamfunction and perturbation vorticity, respectively. Substituting (2.22) and (2.23) into (2.21), we obtain:

$$\begin{aligned}
\nabla^2\left(\frac{\partial}{\partial t}\left[\sum_{|l|\leq N}\left(\hat{\psi}_l e^{il\lambda}\right)\right]\right) &= \frac{1}{r}\Bigg\{\sum_{\substack{|m|\leq N\\ |l|\leq N}}\left[il\frac{\partial}{\partial r}\left(\hat{\zeta}_m\hat{\psi}_l e^{i(m+l)\lambda}\right) - i(m+l)\left(\hat{\zeta}_m e^{i(m+l)\lambda}\frac{\partial\hat{\psi}_l}{\partial r}\right)\right] \\
&+ \sum_{|l|\leq N}\left(il\hat{\psi}_l e^{il\lambda}\right)\frac{\partial\overline{\zeta}}{\partial r} - \sum_{|m|\leq N}\left(im\hat{\zeta}_m e^{im\lambda}\right)\frac{\partial\overline{\psi}}{\partial r}\Bigg\} \\
&+ \nu\nabla^2\left[\sum_{|m|\leq N}\left(\hat{\zeta}_m e^{im\lambda}\right)\right].
\end{aligned} \tag{2.24}$$

Mulitplying Eq. (2.24) by $e^{-in\lambda}$, where n is an arbitrary integer, then yields:

$$\begin{aligned}
\nabla^2\left(\frac{\partial}{\partial t}\left[\sum_{|l|\leq N}\left(\hat{\psi}_l e^{il\lambda}\right)\right]\right)\cdot e^{-in\lambda} &= \frac{1}{r}\Bigg\{\sum_{\substack{|l|\leq N\\ |m|\leq N}}\left(e^{i(m+l-n)\lambda}\left[il\frac{\partial}{\partial r}\left(\hat{\zeta}_m\hat{\psi}_l\right) - i(m+l)\left(\hat{\zeta}_m\frac{\partial\hat{\psi}_l}{\partial r}\right)\right]\right) \\
&+ \sum_{|l|\leq N}\left(il\hat{\psi}_l e^{i(l-n)\lambda}\right)\frac{\partial\overline{\zeta}}{\partial r} - \sum_{|m|\leq N}\left(im\hat{\zeta}_m e^{i(m-n)\lambda}\right)\frac{\partial\overline{\psi}}{\partial r}\Bigg\} \\
&+ \nu\nabla^2\left[\sum_{|m|\leq N}\left(\hat{\zeta}_m e^{im\lambda}\right)\right]\cdot e^{-in\lambda}.
\end{aligned} \tag{2.25}$$

We next azimuthally integrate from $\lambda = 0$ to $\lambda = 2\pi$. Because of the periodic nature of the complex exponential function, the only non-zero terms in this integral are those for which the exponent is zero. Eq. (2.25) therefore reduces to:

$$\nabla_n^2\left(\frac{\partial\hat{\psi}_n}{\partial t}\right) = \frac{1}{r}\Bigg\{\sum_{\substack{|l|\leq N\\ |n-l|\leq N}}\left[il\frac{\partial}{\partial r}\left(\hat{\zeta}_{n-l}\hat{\psi}_l\right) - in\left(\hat{\zeta}_{n-l}\frac{\partial\hat{\psi}_l}{\partial r}\right)\right] + in\hat{\psi}_n\frac{\partial\overline{\zeta}}{\partial r} - in\hat{\zeta}_n\frac{\partial\overline{\psi}}{\partial r}\Bigg\} + \nu\nabla_n^2\hat{\zeta}_n, \tag{2.26}$$

for $n\epsilon\{-N, -N+1, ..., 0, ..., N-1, N\}$. Here

$$\nabla_n^2 = \frac{1}{r}\frac{\partial}{\partial r} + \frac{\partial^2}{\partial r^2} - \frac{n^2}{r^2} \tag{2.27}$$

is the horizontal Laplacian operator in azimuthal Fourier space. Formally inverting our prognostic equation for the streamfunction amplitude yields:

$$\frac{\partial\hat{\psi}_n}{\partial t} = \nabla_n^{-2}\hat{F}_n(r,t) \tag{2.28}$$

where

$$\hat{F}_n(r,t) = \frac{1}{r}\Bigg\{\sum_{\substack{|l|<N\\ |n-l|\leq N}}\left[il\frac{\partial}{\partial r}\left(\hat{\psi}_l\hat{\zeta}_{n-l}\right) - in\hat{\zeta}_{n-l}\frac{\partial\hat{\psi}_l}{\partial r}\right] + in\frac{\partial\overline{\zeta}}{\partial r}\hat{\psi}_n - in\frac{\partial\overline{\psi}}{\partial r}\hat{\zeta}_n\Bigg\} + \nu\nabla_n^2\hat{\zeta}_n. \tag{2.29}$$

Note that a distinction has been made between $\hat{\psi}_0$ and $\hat{\zeta}_0$, and $\overline{\psi}$ and $\overline{\zeta}$. The former are the predicted increments in azimuthal mean streamfunction and vorticity, respectively, from one timestep to the next. These incremental changes are transferred to $\overline{\psi}$ and $\overline{\zeta}$ at the end of each time step, and then set to zero before the next time step. Therefore, terms in (2.29) involving $\hat{\psi}_0$ and $\hat{\zeta}_0$ make no contribution to the sum.

2.7.1 Accuracy of Spatial Derivatives

The radial derivatives in the SS model are specified to be second order accurate and are computed via centered differences. The azimuthal derivatives are by Fourier methods and, as in the SP model, are computed exactly for the given wavenumber truncation.

Inversion of the vorticity for the streamfunction is accomplished via a standard tri-diagonal solver. Unlike the SP model, the number of modes resolved in the azimuthal direction is entirely at the discretion of the user which allows for greater flexibility of the SS model in this regard.

2.7.2 Boundary Conditions

The boundary conditions for the SS model are as follows:

$$\left.\begin{array}{rcl} \frac{\partial}{\partial t}\frac{\partial \hat{\psi}_0}{\partial r}(r,t) & = & 0 \\ \hat{\psi}_{n\neq 0}(r,t) & = & 0 \end{array}\right\} \quad \text{at } r = 0, r_{\max}, \tag{2.30}$$

where $\partial\hat{\psi}_0/\partial r$ is the incremental change in azimuthal mean tangential wind and $\hat{\psi}_n$ is the streamfunction amplitude for wavenumber n. The first boundary condition ensures the conservation of total circulation and forces the basic state winds to remain zero at the center of the vortex (since they are initially set to zero and singularities in the vorticity field are not allowed). The second boundary condition prohibits inflow/outflow across the domain boundary $r = r_{\max}$ and, at the center of the domain, is a result of Taylor expanding the streamfunction about $r = 0$. Since we do not allow singularities at $r = 0$, the expansion requires $\hat{\psi}_{n\neq 0}(r = 0, t) = 0$.

2.7.3 Linearity

The SS model generally performs fully non-linear calculations. However, the non-linear advective terms may be switched off allowing for linear and/or wave-mean flow simulations, a unique characteristic of the SS model.

Linear Simulations

For the linear calculations, we neglect products of perturbation quantities. Consequently, the basic state profile is unchanged (i.e., $\partial\hat{\psi}_0/\partial t = 0$). In this case the governing equation for the asymmetric part of the flow is simply the linearized approximation of Eq. (2.17):

$$\nabla^2\left(\frac{\partial \psi'}{\partial t}\right) = \frac{1}{r}\frac{\partial \psi'}{\partial \lambda}\frac{\partial \overline{\zeta}}{\partial r} - \frac{1}{r}\frac{\partial \overline{\psi}}{\partial r}\frac{\partial \zeta'}{\partial \lambda} + \nu\nabla^2\zeta'. \tag{2.31}$$

In (2.31), the cylindrical polar geometry of the model provides a physically useful linear limit that is natural for vortex dynamics problems. In azimuthal spectral space, the governing equations for the asymmetric ($n \neq 0$) modes are:

$$\nabla_n^2\left(\frac{\partial \hat{\psi}_n}{\partial t}\right) = \frac{1}{r}\left(in\hat{\psi}_n\frac{\partial \overline{\zeta}}{\partial r} - in\hat{\zeta}_n\frac{\partial \overline{\psi}}{\partial r}\right) + \nu\nabla_n^2\hat{\zeta}_n. \tag{2.32}$$

Wave-Mean Flow Simulations

For the wave-mean flow calculations we allow the basic state to be modified through the self-interaction of azimuthal modes, but prohibit the interaction of modes with different azimuthal wavenumbers. The governing equations in this case are as follows. For $n \neq 0$,

$$\nabla_n^2\left(\frac{\partial\hat{\psi}_n}{\partial t}\right) = \frac{1}{r}\left(in\hat{\psi}_n\frac{\partial\overline{\zeta}}{\partial r} - in\hat{\zeta}_n\frac{\partial\overline{\psi}}{\partial r}\right) + \nu\nabla_n^2\hat{\zeta}_n, \tag{2.33}$$

while for $n = 0$,

$$\nabla_0^2\frac{\partial\psi_0}{\partial t} = \frac{1}{r}\sum_{|l|\leq N}\left[il\frac{\partial}{\partial r}\left(\hat{\zeta}_{-l}\hat{\psi}_l\right)\right]. \tag{2.34}$$

Chapter 3

AXISYMMETRIZATION OF NEARBY VORTICITY ANOMALIES ON A MONOPOLAR VORTEX

3.1 Introduction

In this chapter, we present the results of the first set of experiments performed on the three models. The physical problem being studied is the axisymmetrization of nearby vorticity anomalies on a basic state vortex whose initial vorticity distribution decreases monotonically and smoothly with radius. This particular choice of basic state can be likened to a developing tropical depression, while the vorticity perturbation is intended to be a parametrization of the cyclonic vorticity produced by a convective "blow-up" near the radius of maximum winds (RMW) of the incipient basic state vortex (Gray, 1998; ME). As MK predicted and ME later verified, such a perturbation near a vortex monopole will excite vortex Rossby waves which disperse on the vortex monopole and progressively become sheared by the mean swirling vortex flow. As the waves disperse, they spin-up the interior of the parent vortex by ingesting like sign vorticity toward the center and spin-down the periphery of the vortex by ejecting opposite sign and like sign vorticity to the periphery as vorticity filaments that orbit the vortex. The goal of this set of experiments, then, is to determine if the SS model correctly simulates the axisymmetrization process as well as the interaction of the waves with each other and with the mean flow. We accomplish this goal by examining several diagnostic quantities from the simulations including domain plots of the total vorticity field, radial plots of the changes in mean quantities, and plots of domain-integrated quantities (i.e., total energy, enstrophy, angular momentum, and palinstrophy) as functions of time. Finally, we present statistics regarding the amount of

computer time required for each run. Based on these results, we give an assessment of the SS model's effectiveness for this type of vortex flow.

3.2 Initialization

3.2.1 Basic State

The basic state used for this experiment is a Gaussian-shaped vorticity monopole given by:

$$\overline{\zeta}(r) = \overline{\zeta}_{\max} e^{-(r/r_{\text{decay}})^2}, \tag{3.1}$$

where r is the radius from the center of the vortex, $\overline{\zeta}_{\max} = 1.0 \times 10^{-3}$ s^{-1}, and $r_{\text{decay}} = 47$ km. This choice of parameters yields a vortex possessing maximum tangential winds of 16.5 ms^{-1} at a radius of approximately 60 km (see Fig. 3.1a) and a minimum central pressure of approximately 991 mb (Fig. 3.1d), not unlike typical values for a tropical depression.

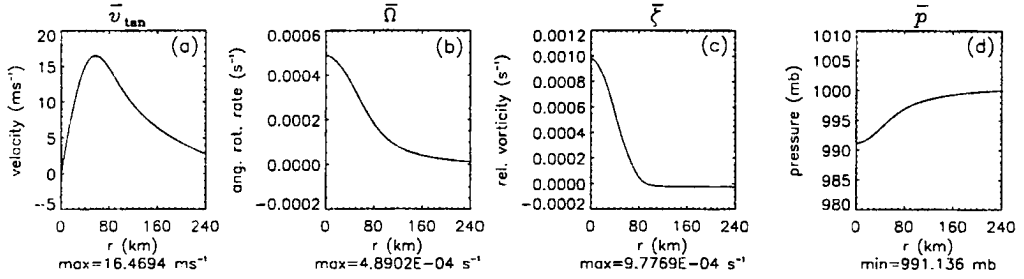

Figure 3.1: Initial profiles of azimuthal mean (a) tangential winds ($\overline{v}_{\text{tan}}$), (b) angular rotation rate ($\overline{\Omega} = \overline{v}_{\text{tan}}/r$), (c) relative vorticity ($\overline{\zeta}$), and (d) pressure ($\overline{p}$) as functions of radius from the center of the parent vortex. All models are initialized with the mean vorticity profile given in (c). The remaining quantities are diagnosed from the $\overline{\zeta}$ profile.

3.2.2 Stability Characteristics of the Monopole Profile

Since the basic state radial vorticity gradient does not change sign as one proceeds from the center outward, the basic state satisfies Rayleigh's sufficient condition for exponential stability (Gent and McWilliams, 1986; see Fig. 3.2 for a plot of $d\overline{\zeta}/dr$). This does not mean that perturbations to the vorticity cannot initiate wave activity within the flow.

Indeed, MK predicted and ME verified that perturbations to the basic state initiate outward propagating vortex Rossby waves that redistribute the vorticity perturbation as the vortex equilibrates. In the process, perturbation cyclonic vorticity is transported inward and perturbation cyclonic and anticyclonic vorticity is ejected outward. Together, this spins-up the interior and spins-down the periphery of the vortex.

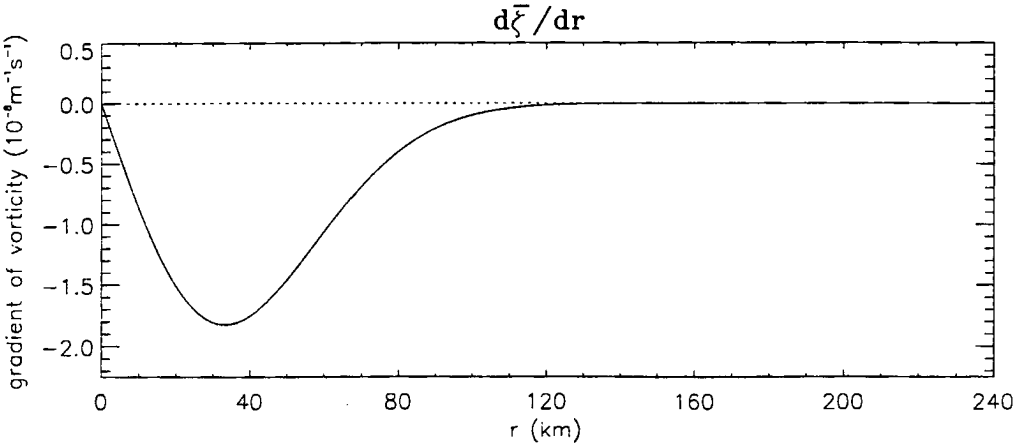

Figure 3.2: Gradient of vorticity for the monopole experiments.

3.2.3 Vortex Rossby Waves

As evident from Figs. 3.1c and 3.2, the radial gradient of initial basic state vorticity is smooth and nonzero out to a radius of approximately 120 km from the center of the vortex. Much like planetary Rossby waves that owe their existence to the non-zero gradient of planetary vorticity, vortex Rossby waves should exist in this region where $d\bar{\zeta}/dr \neq 0$. The restoring mechanism for vortex Rossby waves is the gradient of storm relative vorticity, or the so-called Rossby restoring mechanism (MK; Guinn and Schubert, 1993–henceforth GS). It was shown in GS, MK, and ME that these waves will tend to resist departures from axisymmetry (i.e., perturbations) until they are sheared by the mean flow. During this time, the waves redistribute perturbation vorticity until an axisymmetric (or nearly-axisymmetric) state is established.

3.2.4 Perturbation

To study vortex Rossby waves, we introduce a vorticity anomaly to the basic state flow. This is a reasonable course of action since we are simulating the dynamics of a

developing tropical depression. As such, we simulate the effects of convection that are likely to occur in the domain of the vortex. ME showed that a convective burst in a hurricane-type vortex can be idealized by an impulse of cyclonic vorticity in the lower troposphere. Following in this vein, our perturbation vorticity profile is a Gaussian with a similar structure as Eq. (3.1) but with the perturbation maximum ($\zeta'_{\max}$) and radius of decay (r_{decay}) adjusted as follows:

$$\left.\begin{array}{c} \zeta'_{\max} = \frac{1}{2}\overline{\zeta}_{\max} \\ r_{\text{decay}}(\text{perturbation}) = \frac{2}{3} r_{\text{decay}}(\text{basic state}). \end{array}\right\} \tag{3.2}$$

See Figs. 3.3b,c for plots of Eq. (3.2) and the total field of vorticity ($\zeta = \overline{\zeta} + \zeta'$). Note the maximum of ζ' is 0.5 $\overline{\zeta}_{\max}$, a finite amplitude perturbation relative to the basic state, with a shorter e-folding distance. Also note that the maximum of ζ' is located just inside the RMW indicated by the dashed line in Fig. 3.3b.

3.3 Model Setup

The following table summarizes the numerical parameters used in the monopole experiment for the FD, SP, and SS models:

	FD	**SP**	**SS**
Viscosity (ν)	100 m^2s^{-1}	100 m^2s^{-1}	100 m^2s^{-1}
No. gridpoints	x: 300, y: 300	x: 300, y: 300	r: 426
Gridspacing	$dx = dy = 2$ km	$dx = dy = 2$ km	$dr = 1$ km
No. of modes	n/a	x:100, y:100	λ:16
Timestep	30 s	30 s	30 s
Degrees of Freedom	$(300)^2 = 90,000$	$(300)^2 = 90,000$	(426)(32)=13,632

Table 3.1: Numerical parameters used in the SP, FD, and SS models for the monopole experiments.

Although we present grid spacings for the SP model in Table 3.1, a more realistic estimate of the resolution is the wavelength of the smallest resolvable Fourier mode (3 times the grid spacing; S99, Sect. 3) which is 6 km.

In the SS model, a more realistic estimate of the resolution in the azimuthal direction is the wavelength of the smallest resolvable Fourier mode at the RMW. For the monopole,

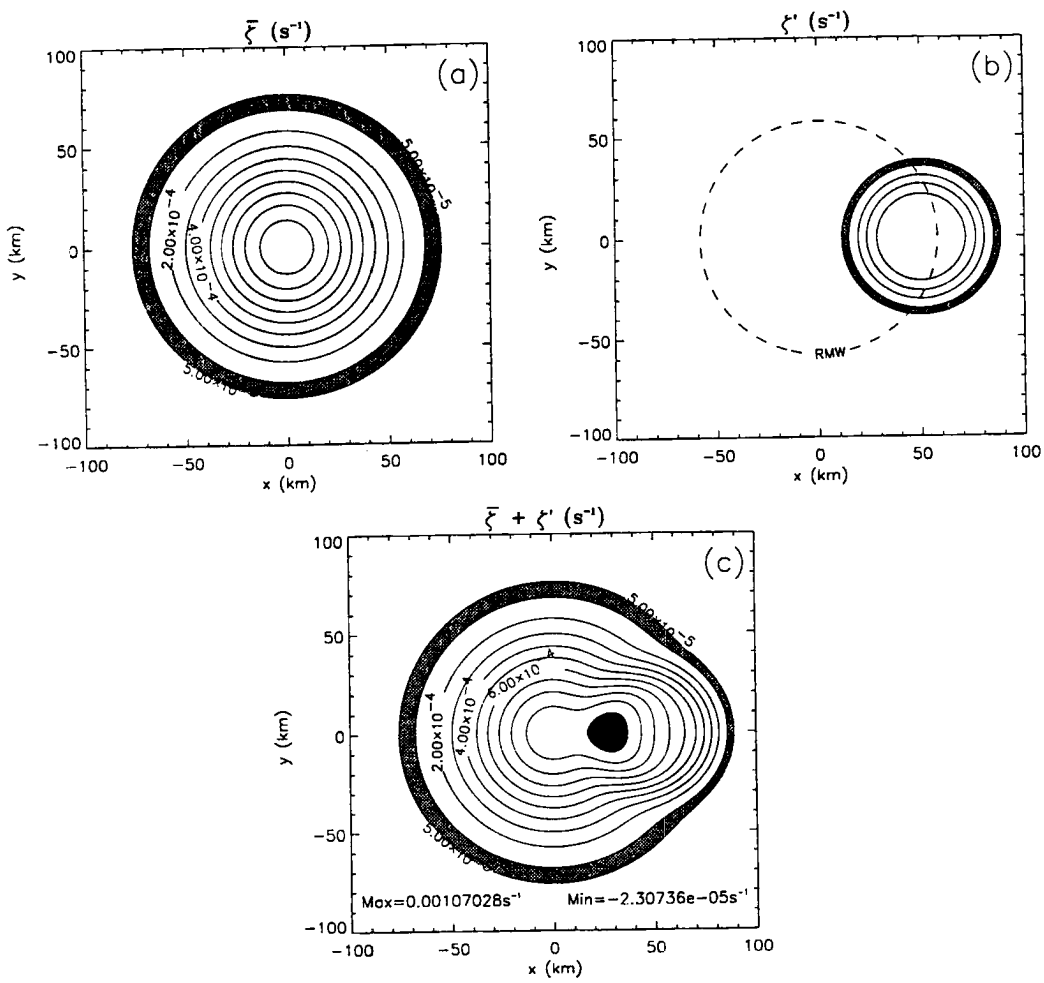

Figure 3.3: Initial plots of (a) basic state, (b) perturbation and (c) total relative vorticity as functions of x and y over a 200 km $\times$ 200 km subset of the entire domain. The lowest contour level is 5.0×10^{-5} s^{-1} with the remaining contour levels beginning at 1.0×10^{-4} s^{-1} in increments of 1.0×10^{-4} s^{-1}. Grey indicates 5.0×10^{-5} s^{-1} $\leq \zeta \leq 1.0 \times 10^{-4}$ s^{-1}, and black indicates $\zeta \geq 10.0 \times 10^{-4}$ s^{-1}. $\bar{\zeta}_{\max} = 1.0 \times 10^{-3}$ s^{-1} and $\zeta'_{\max} = 0.5 \times 10^{-3}$ s^{-1}.

this is approximately 22.8 km. In the radial direction, we assume the wavelength of the smallest resolvable mode is 4 times the radial grid spacing. This yields an effective radial resolution of 4 km for the SS model.

In the FD model, we also assume the wavelength of the smallest resolvable Fourier mode is 4 times the grid spacing. This yields an effective resolution of 8 km.

3.4 Expected Results

As a result of our perturbation and due to the restoring mechanism resisting departures from axisymmetry, we expect to see vortex Rossby waves develop in the flow. These waves will then transport anomalously high vorticity toward the center of the vortex and anomalously low and high vorticity outward to the edges of the domain in the process of equilibrating. As the waves propagate outward, we expect that they will become progressively sheared by the differential rotation rate of the basic state vortex (MK).

Furthermore, we expect to see a spin-up of the vortex if we examine plots of changes in mean quantities over the course of the simulation. This spin-up (as predicted by MK and verified by ME) should occur near the radius of the asymmetry and should be accompanied by a smaller but notable spin-down at larger radii.

3.5 Results

3.5.1 Nonlinear Runs

The following figures show the results of this first set of experiments. The FD model results are shown first followed by the SP and the SS models. In all cases, we plot data for a 200 km $\times$ 200 km subset of the entire domain. We concentrate only on the region of the vortex where most of the dynamics occur.

We examine first the evolution of the total vorticity field given by Figs. 3.4, 3.5 and 3.6. Immediately, we see that all three models are producing nearly identical results. One would expect this to be the case for the FD and SP plots since these models are formulated on Cartesian grids with exactly the same structure. However, what is surprising is the striking similarity between the SS and SP schemes. One might not expect such agreement

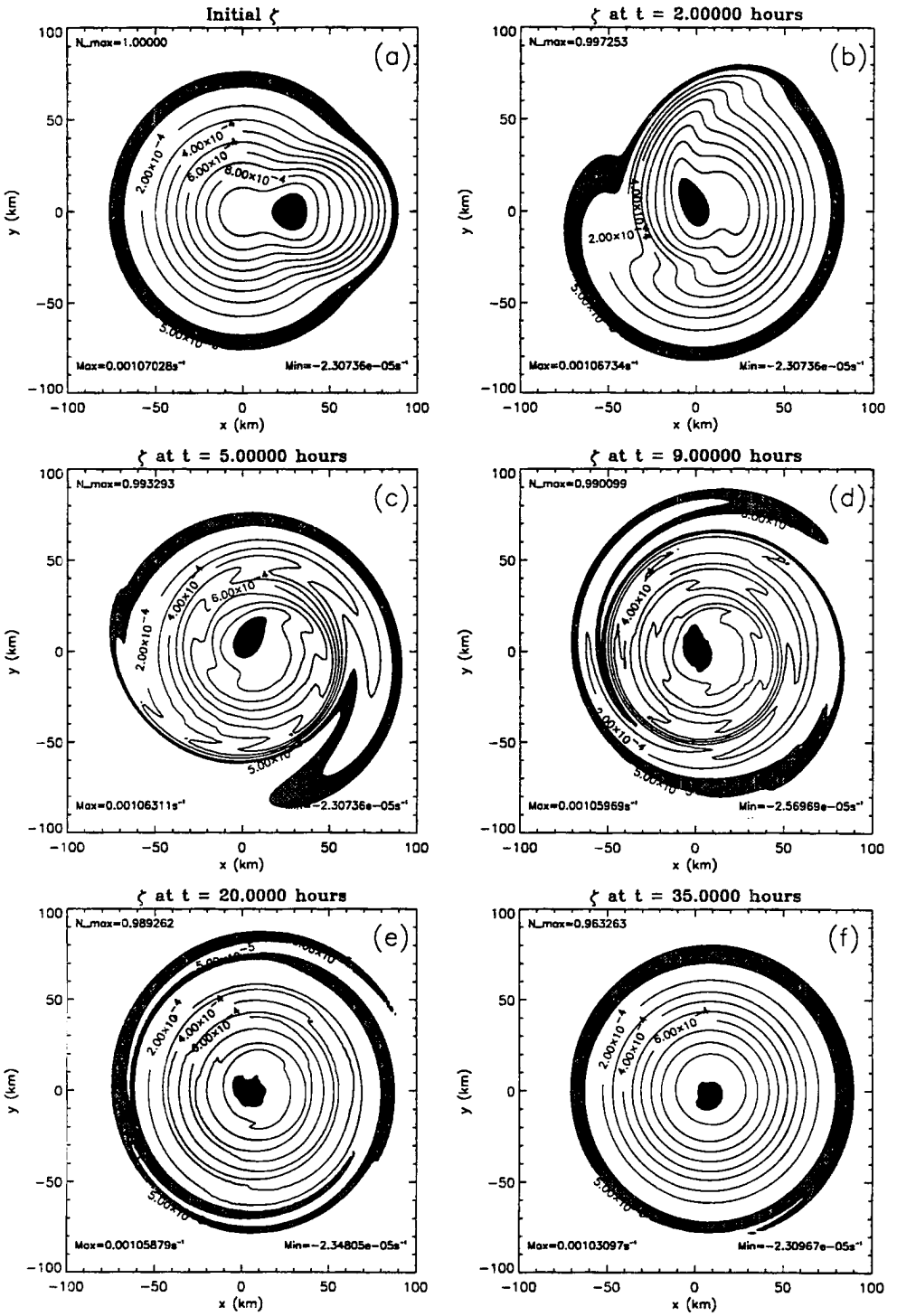

Figure 3.4: FD model vorticity evolution for the perturbed monopole experiment. In each panel, a 200 km × 200 km subset of the entire domain is plotted. The lowest contour level is 5.0×10^{-5} s^{-1} with the remaining contour levels beginning at 1.0×10^{-4} s^{-1} in increments of 1.0×10^{-4} s^{-1}. Grey indicates 5.0×10^{-5} s^{-1} $\leq \zeta \leq 1.0 \times 10^{-4}$ s^{-1}, and black indicates $\zeta \geq 10.0 \times 10^{-4}$ s^{-1}.

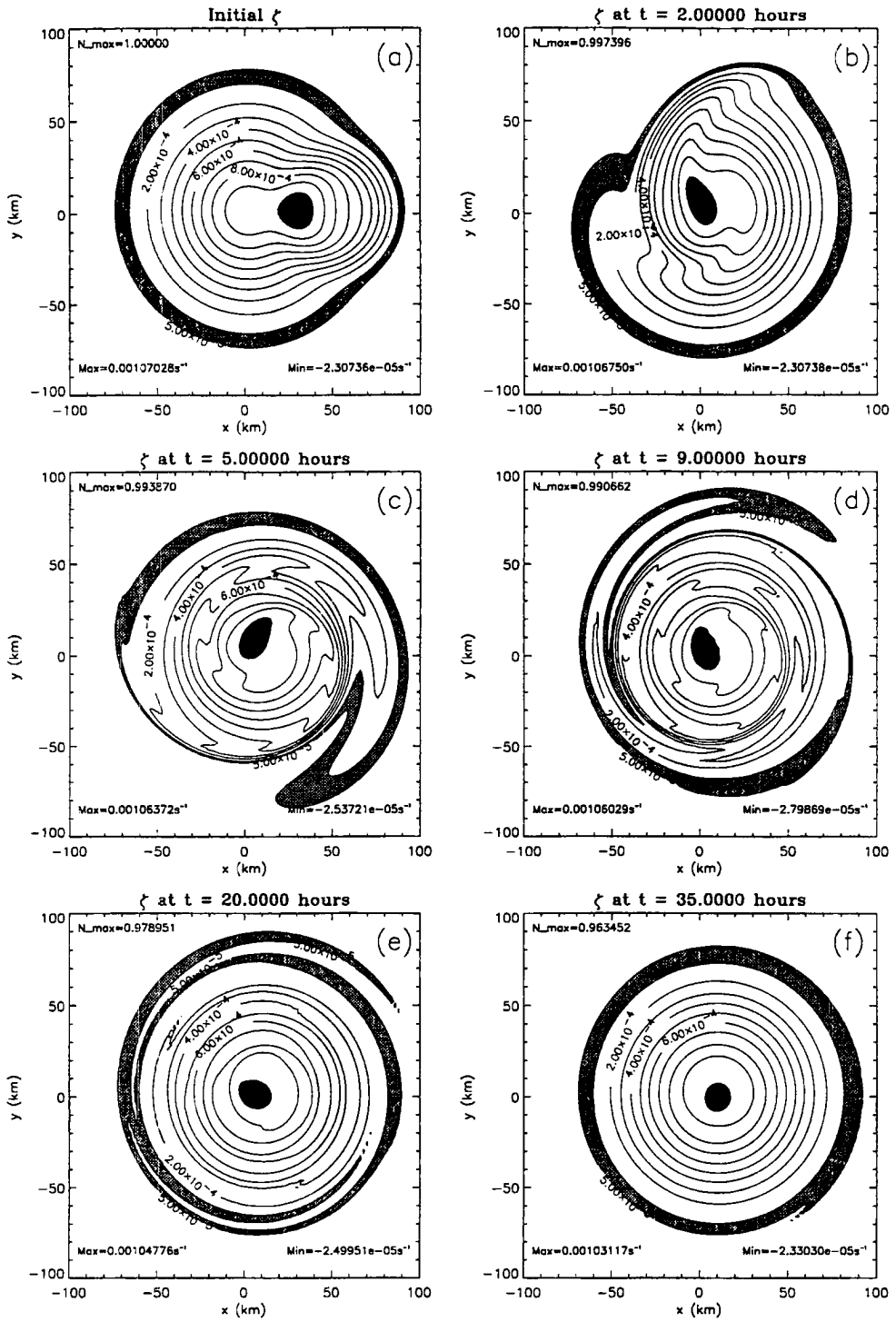

Figure 3.5: SP model vorticity evolution for the perturbed monopole experiment. In each panel, a 200 km × 200 km subset of the entire domain is plotted. The lowest contour level is 5.0×10^{-5} s^{-1} with the remaining contour levels beginning at 1.0×10^{-4} s^{-1} in increments of 1.0×10^{-4} s^{-1}. Grey indicates 5.0×10^{-5} s^{-1} $\leq \zeta \leq 1.0 \times 10^{-4}$ s^{-1}, and black indicates $\zeta \geq 10.0 \times 10^{-4}$ s^{-1}.

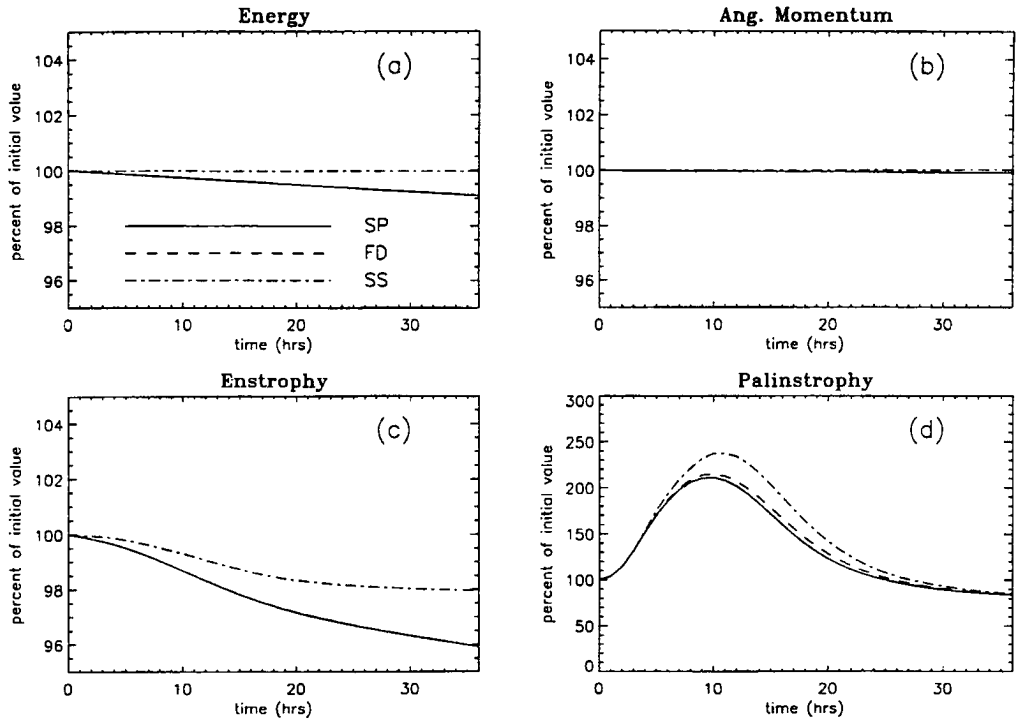

Figure 3.7: Time evolution of integrated (a) total energy ($E = \int\int \frac{1}{2} \nabla \psi \cdot \nabla \psi \, dA$), (b) angular momentum ($AM = \int\int r^2 \zeta \, dA$), (c) enstrophy ($V = \int\int \frac{1}{2} \zeta^2 \, dA$), and (d) palinstrophy ($P = \int\int \frac{1}{2} \nabla \zeta \cdot \nabla \zeta \, dA$) over the course of the run for the SP model (solid), FD model (dashed), and SS model (dash-dot). Values are normalized based on the initial value. Note the scale changes from (c) to (d). In (a), (b), and (c) the FD curve is not visible because it is covered by the SP curve.

3.8). As expected, we see a spin-up of the vortex near the radius of the initial asymmetry due to vortex Rossby wave dynamics. If we compare all three models, we again find virtually identical results. Granted, there are some differences in the shapes of the curves and their maximum values, but these differences are slight. Note the maximum spin-up in all three cases (as measured by $\Delta\overline{v}$) is approximately 0.4 ms^{-1}. Also noteworthy is the plot of $\Delta\overline{\zeta}$ which shows that high vorticity is transported inward near the center of the vortex, and low and high vorticity is ejected outward past the radius of the initial asymmetry. This has been confirmed by analyzing Lagrangian trajectories of particles placed within the fluid (not shown).

From the above analysis the SS model appears to give reliable results for the axisymmetrization of nearby vorticity anomalies.

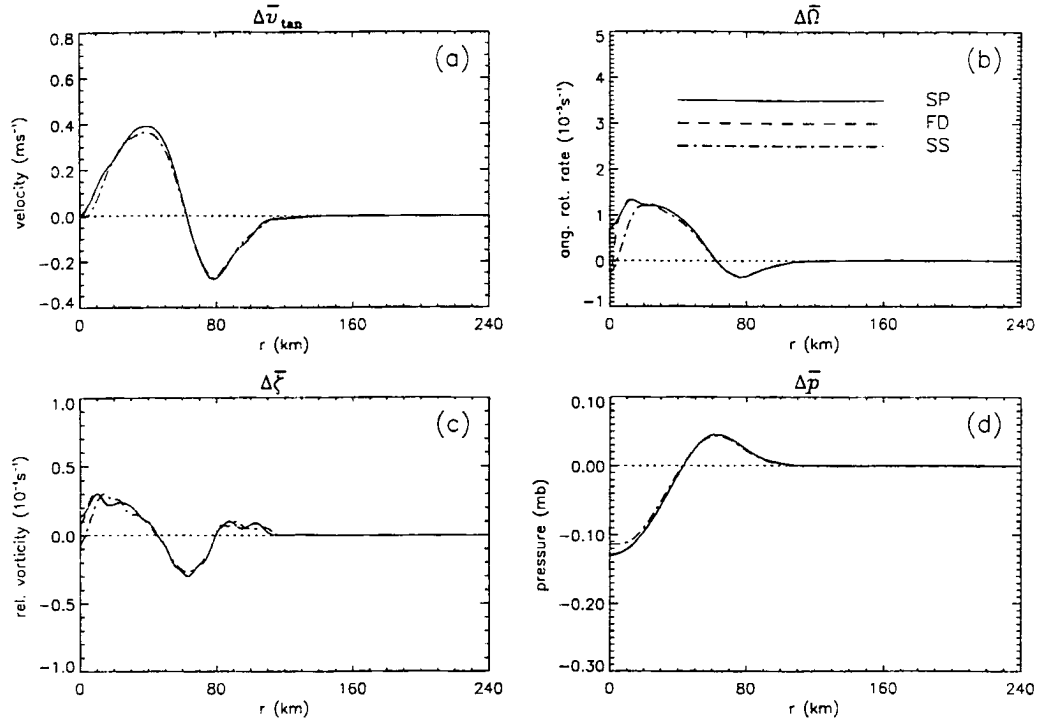

Figure 3.8: Changes in the azimuthal mean (a) tangential wind ($\overline{v}_{\tan}$), (b) angular rotation rate ($\overline{\Omega}$), (c) vorticity ($\overline{\zeta}$), and (d) pressure ($\overline{p}$) over the course of the run for the SP model (solid), FD model (dashed), and the SS model (dash-dot). Note the units for the $\overline{\Omega}$ and the $\overline{\zeta}$ plots are 10^{-5} s^{-1} and 10^{-4} s^{-1}, respectively. In all panels, the FD curve is not visible because it is covered by the SP curve.

3.5.2 Linear and Wave-Mean Flow Runs

In addition to the fully nonlinear calculations performed by each model, we also performed linear and wave-mean flow calculations using the SS model. Figs. 3.9 and 3.10 show the evolution of the vorticity field for the linear and wave-mean flow experiments, respectively. Comparing these figures with the field plots of the nonlinear evolution (Figs. 3.4, 3.5, and 3.6), we see a strong similarity. Just as in plots of the nonlinear simulation, vortex Rossby waves develop and redistribute the vorticity field such that high vorticity is transported inward and low and high vorticity is ejected outward in the process of equilibrating to an approximate monopole. However, the linear and wave-mean flow dynamics are not able to fully resolve the region of highest vorticity (black). This is to be expected since wave-wave interactions are not allowed in the linear run, and wave interactions with the basic state only are allowed in the wave-mean flow run.

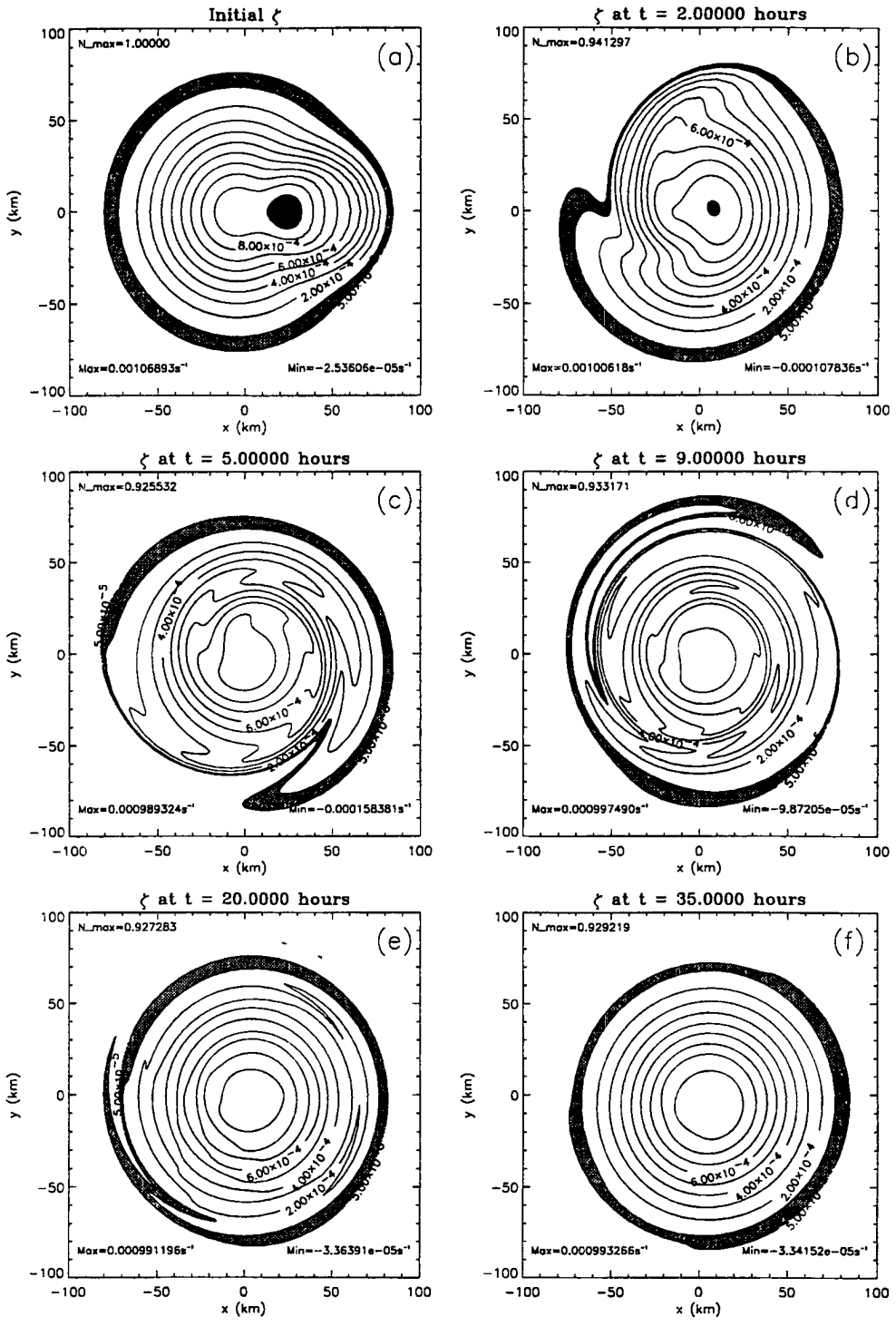

Figure 3.9: Linear evolution of the perturbed monopole as simulated in the SS model. In each panel, a 200 km × 200 km subset of the entire domain is plotted. The lowest contour level is 5.0×10^{-5} s^{-1} with the remaining contour levels beginning at 1.0×10^{-4} s^{-1} in increments of 1.0×10^{-4} s^{-1}. Grey indicates 5.0×10^{-5} s^{-1} $\leq \zeta \leq 1.0 \times 10^{-4}$ s^{-1}, and black indicates $\zeta \geq 10.0 \times 10^{-4}$ s^{-1}.

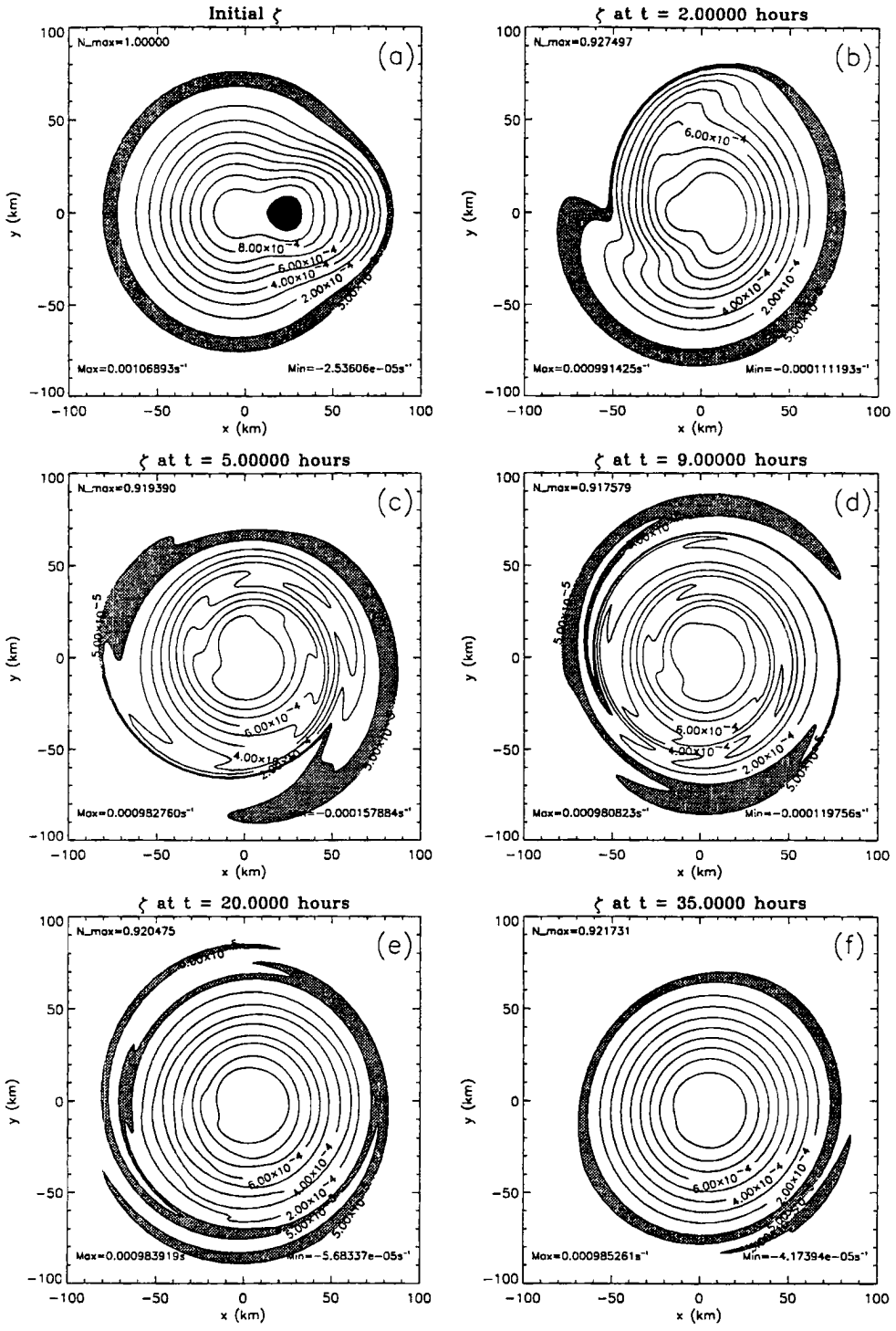

Figure 3.10: Wave-mean flow evolution of the perturbed monopole as simulated in the SS model. In each panel, a 200 km × 200 km subset of the entire domain is plotted. The lowest contour level is 5.0×10^{-5} s^{-1} with the remaining contour levels beginning at 1.0×10^{-4} s^{-1} in increments of 1.0×10^{-4} s^{-1}. Grey indicates 5.0×10^{-5} s^{-1} $\leq \zeta \leq 1.0 \times 10^{-4}$ s^{-1}, and black indicates $\zeta \geq 10.0 \times 10^{-4}$ s^{-1}.

On the whole, though, the wave-mean flow and linear dynamics are reproducing the basic aspects of the vortex evolution. This result suggests that the dynamics of the monopole vortex are mostly linear in nature. We might also expect this to be the case for even larger amplitude perturbations, with a small caveat. If the maximum of the perturbation were twice the basic state maximum, the resultant vorticity field would evolve as though the perturbation (since it is larger in amplitude) were actually the basic state and the basic state actually the perturbation. In this case, we would see an evolution nearly identical to the monopole case just presented (assuming the spatial scales are the same).

3.5.3 Timing Data

MODEL	RUN TIME (CPU)
SP	579 min
FD	2272 min
SS	248 min

Table 3.2: Timing data for the three monopole runs based on the amount of CPU time required for each to run to completion for a 35 h vortex simulation.

We finally examine timing statistics for each run. The SS model is able to run to completion in nearly half the time required by the SP model and nearly one-tenth that required by the FD model for the numerical parameters chosen.

3.6 Tropical Depression Simulation Conclusions

Based on the timing statistics and the fact that the results among all three models are nearly identical, we conclude that the semi-spectral formulation is at least as good as, if not superior to, traditional formulations in simulating the axisymmetrization of finite amplitude vorticity anomalies near the RMW of a monopole vortex.

Chapter 4

RING VORTEX

4.1 Introduction

In Chapter 3 we found that the SS model yielded nearly identical results to the FD and SP models for the case of a circular vortex monopole perturbed by a finite amplitude vorticity anomaly near the RMW of the parent vortex. As far as timing considerations are concerned, the SS model strongly outperformed the FD model and was competitive with the SP model for the numerical parameters chosen.

A more extreme test of the SS model is furnished by examining the problem of barotropic instability and breakdown of an idealized hurricane-like vortex. For our purpose, the hurricane-like vortex is modeled as a ring of elevated vorticity just inside the RMW. Eliassen and Lystad (1977) showed that the maximum vertical velocity at the top of the boundary layer in a hurricane is located just inside the RMW due to frictional stress. Convection is organized by the vertical velocity into an annular ring near the RMW. The convection induces vortex stretching which enhances the vorticity in the ring and leads to an area of strong cyclonic shear on the inner edge of the convection. This shear zone can be thought of as a ring of elevated vorticity with sharp gradients on its edges (S99). Unlike the perturbed monopole, the vorticity dynamics of this vortex are highly nonlinear and lead to extensive vorticity mixing with repeated stretching and folding of vorticity contours, an extreme testbed for the SS model.

Since the FD model was significantly slower than both the SP and FD models in the previous experiment, we elect not to simulate the evolution of the vortex ring with the FD model. This is justifiable because the baseline performance of each model and the

relative performance characteristics between models have already been determined with the perturbed monopole experiment.

4.2 Initialization

4.2.1 Basic State

In this set of experiments, we simulate the unforced evolution of a perturbed hurricane-like vortex possessing a ring of elevated cyclonic vorticity just inside the RMW. To yield a vortex possessing hurricane-strength winds, we desire a radial profile of vorticity that results in maximum tangential winds of approximately 55 ms^{-1} at a radius near 30 km.

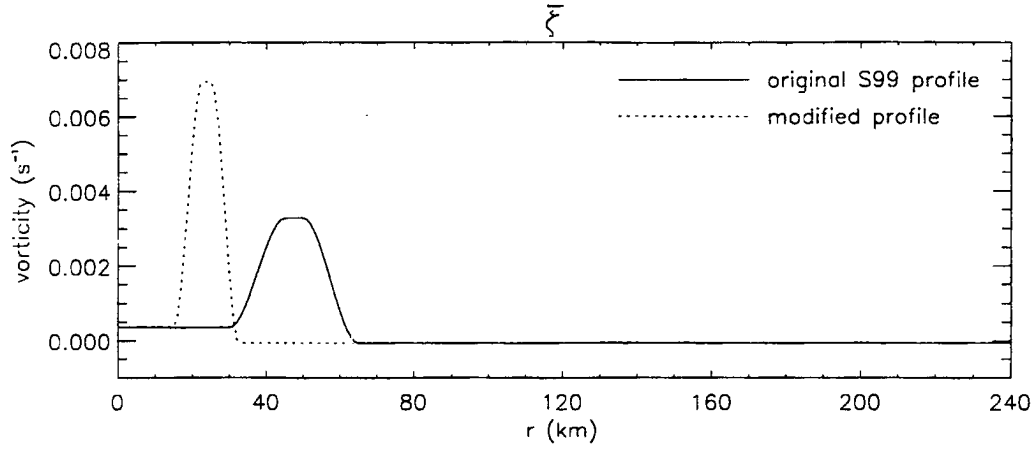

Figure 4.1: Original (S99) and modified radial profiles of $\overline{\zeta}$. The maximum value of $\overline{\zeta}$ in the elevated region for the modified profile is a little more than twice that of the original profile.

A similar but larger vortex was used in S99 consisting of a continuous distribution of vorticity with low values in a region near the center, high values in a region centered around 50 km, and zero values beyond that radius (see Fig. 4.1, solid curve). This "elevated ring" profile results in maximum tangential winds of approximately 55 ms^{-1} at an RMW near 60 km. In order to obtain an RMW of 30 km while preserving the essential characteristics inherent with the S99 profile, we modified the radial distribution such that the non-zero vorticity values occurred over half the radial distance as the original profile and still yielded the desired 55 ms^{-1} maximum tangential winds. This latter property was fulfilled

by increasing the maximum vorticity in the ring to nearly twice the value used by S99 (see Figs. 4.1 and 4.2).

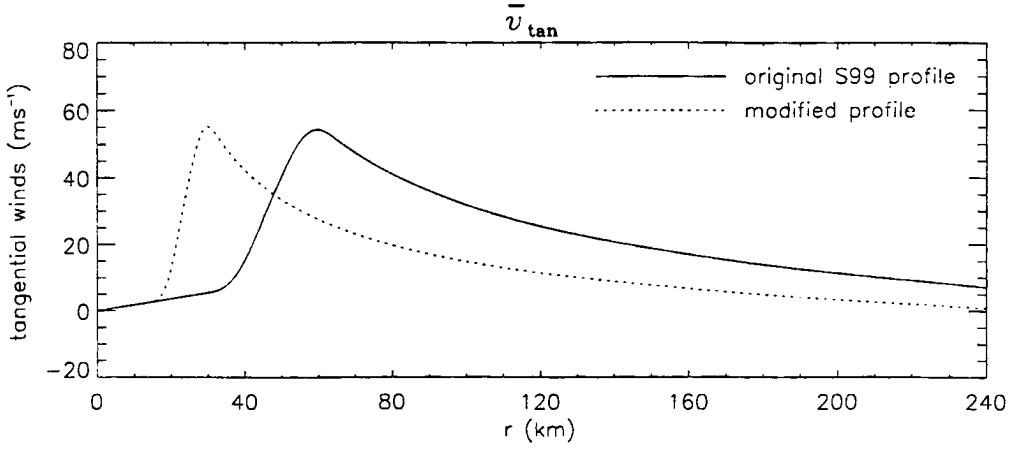

Figure 4.2: Radial profiles of $\overline{v}_{\tan}$ resulting from Fig. 4.1. The maximum values are approximately equal, while the RMW for the modified profile is near 30 km compared near 60 km for the original profile.

The function used to create the smooth distribution of $\overline{\zeta}$ shown in Fig. 4.1 is:

$$\overline{\zeta}(r, t=0) = \begin{cases} \zeta_1, & 0 \le r \le r_1 - d_1 \\ \zeta_1 S((r - r_1 + d_1)/2d_1) + \zeta_2 S((r_1 + d_1 - r)/2d_1), & r_1 - d_1 \le r \le r_1 + d_1 \\ \zeta_2, & r_1 + d_1 \le r \le r_2 - d_2 \\ \zeta_2 S((r - r_2 + d_2)/2d_2), & r_2 - d_2 \le r \le r_2 + d_2 \\ 0, & r_2 + d_2 \le r \le \infty, \end{cases} \tag{4.1}$$

where r_1, r_2, d_1, d_2, ζ_1, and ζ_2 are specified constants. In our case $r_1 = 18.75$ km, $r_2 = 28.75$ km, $d_1 = d_2 = 3.75$ km, $\zeta_1 = 4.1825 \times 10^{-4}$ s^{-1}, and $\zeta_2 = 7.0 \times 10^{-3}$ s^{-1}. Also, $S(s) = 1 - 3s^2 + 2s^3$ is a function satisfying $S(0) = 1$, $S(1) = 0$, $S'(0) = 0$, and $S'(1) = 0$, which guarantees the profile and the first derivative of the profile are continuous at the transition points (S99). See Fig. 4.3 for the corresponding initial profiles of $\overline{v}_{\tan}(r)$, $\overline{\Omega}(r)$, and $\overline{p}(r)$.

In S99 two parameters of the basic state profile surfaced as being key to delineating the stability characteristics of the vortex. These parameters are $\delta = r_1/r_2$ and $\gamma = \zeta_1/\zeta_{\text{av}}$, where $\zeta_{\text{av}} = 2v_{\tan}(r_2)/r_2$. For the original S99 profile, $\delta \approx 0.652$ and $\gamma \approx 0.20$, while for the modified profile $\delta \approx 0.652$ and $\gamma \approx 0.10$. Based on Fig. 2 of S99, a plot of dimensionless

growth rates in (δ, γ) space, these parameters predict the most unstable mode for the original S99 profile will be a superposition of $n = 3$ and $n = 4$, while, for the modified profile, the most unstable mode is predicted to be $n = 3$.

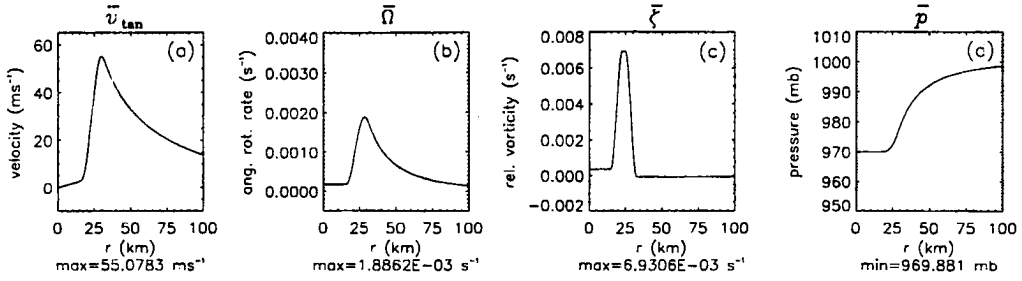

Figure 4.3: Initial profiles of azimuthal mean (a) tangential winds ($\overline{v}_{\tan}$), (b) angular rotation rate ($\overline{\Omega} = \overline{v}_{\tan}/r$), (c) relative vorticity ($\overline{\zeta}$), and (d) pressure ($\overline{p}$) as functions of radius from the center of the vortex. The SP and SS models were initialized with the vorticity profile given in (c). The remaining quantities were inferred from the $\overline{\zeta}$ profile.

4.2.2 Stability Analysis of Vortex Ring Profile

Rayleigh's and Fjørtoft's Theorems

In order to assess the stability of the basic state vortex, we first determine whether the necessary conditions for barotropic instability are met. If these conditions are satisfied, the ring vortex is then potentially unstable to small amplitude perturbations. If any one of the conditions is not met, the profile will be exponentially stable.

We begin with the first of these conditions known as Rayleigh's theorem (Rayleigh, 1880). When applied to a circular basic state flow, Rayleigh's theorem says that for exponential instability, the radial vorticity gradient $d\overline{\zeta}/dr$ must change sign at least once in the flow. The profile of $d\overline{\zeta}/dr$ (Fig. 4.4a) shows that the radial vorticity gradient is positive inside the ring and negative outside, thereby satisfying the necessary condition.

The second condition is known as Fjørtoft's theorem (Fjørtoft, 1950). When applied to a circular basic state flow, the necessary condition is:

$$(\overline{\Omega}(r) - \overline{\Omega}_s)\frac{d}{dr}\overline{\zeta}(r) < 0, \tag{4.2}$$

somewhere in the flow (Edwards, 1994; Gent and McWilliams, 1986). Here $\overline{\Omega}(r)$ is the mean angular rotation rate at radius r, and $\overline{\Omega}_s = \overline{\Omega}(r_s)$ is the mean angular rotation rate at the radius r_s where the mean vorticity gradient changes sign (i.e., $d\overline{\zeta}/dr = 0$).

From Fig. 4.4a, we see that $d\overline{\zeta}/dr = 0$ at a radius of approximately $r = 24$ km. Figure 4.4b is a plot of $\overline{\Omega}(r) - \overline{\Omega}(r = 24 \text{ km})$. Upon examining Figs. 4.4a and b, it is apparent that (4.2) holds in two distinct regions, 15 km $\leq r \leq$ 23 km and 25 km $\leq r \leq$ 33 km. Thus, Fjørtoft's necessary condition is also met.

Interpretation of Necessary Conditions by Vortex Rossby Wave Theory

As we noted in the previous subsection, the radial profile of $d\overline{\zeta}/dr$ (Fig. 4.4a) indicates that the gradient of storm relative vorticity is non-zero in two distinct regions of the initial basic state profile. More precisely:

$$\left.\begin{array}{ll} \frac{d}{dr}\overline{\zeta} > 0, & 15 \text{ km} \leq r < 23 \text{ km} \\ \frac{d}{dr}\overline{\zeta} < 0, & 25 \text{ km} < r \leq 33 \text{ km.} \end{array}\right\} \tag{4.3}$$

Since $d\overline{\zeta}/dr \neq 0$ as indicated in Eq. (4.3) above, if the flow is perturbed we expect to see vortex Rossby waves propagating in these two regions. Furthermore, since the sign of $d\overline{\zeta}/dr$ is opposite in these two regions, we expect to see counter-propagating vortex Rossby waves. In the inner region (15 km $\leq r <$ 23 km), the waves will tend to prograde relative to $\overline{v}_{\tan}$ and, in the outer region (23 km $< r \leq$ 32 km), retrograde relative to $\overline{v}_{\tan}$. When the angular rotation rates of the two wave types are the same, phase locking can occur, and, if properly configured, the two waves can amplify each other (S99). This is the essence of barotropic instability.

Unstable vortex Rossby waves excited in the flow are then the vehicles that initiate the process of redistributing the fluid into a stable monopole.

Eigen-Analysis

To determine the most unstable perturbations, we perform an eigen-analysis of our initial basic state profile following the numerical method of Gent and McWilliams (1986). Assuming modal solutions for the perturbation streamfunction and vorticity:

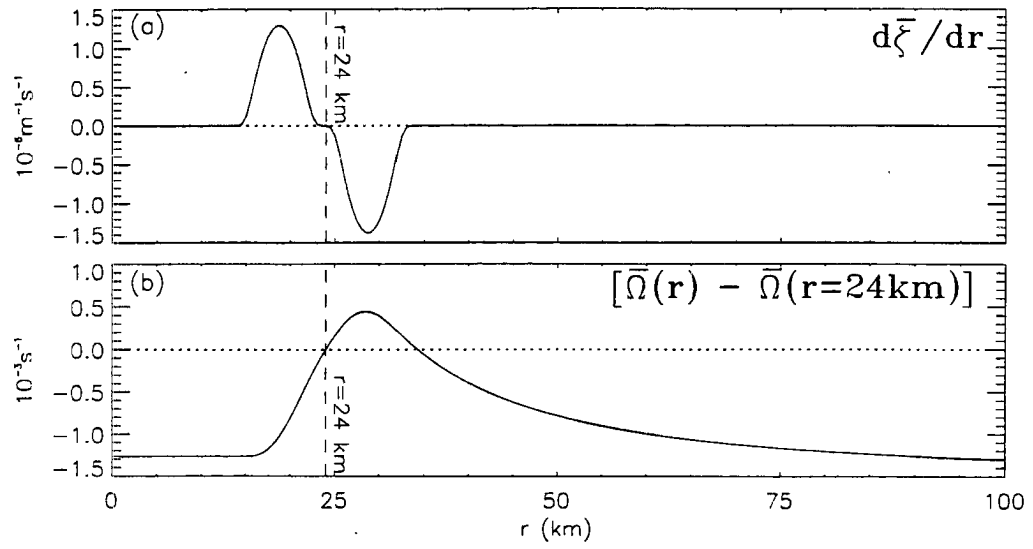

Figure 4.4: Plots of (a) gradient of storm vorticity ($d\overline{\zeta}/dr$) and (b) $\overline{\Omega}(r) - \overline{\Omega}(r = 24$ km) for the modified profile. The dashed vertical line show the location where r=24 km.

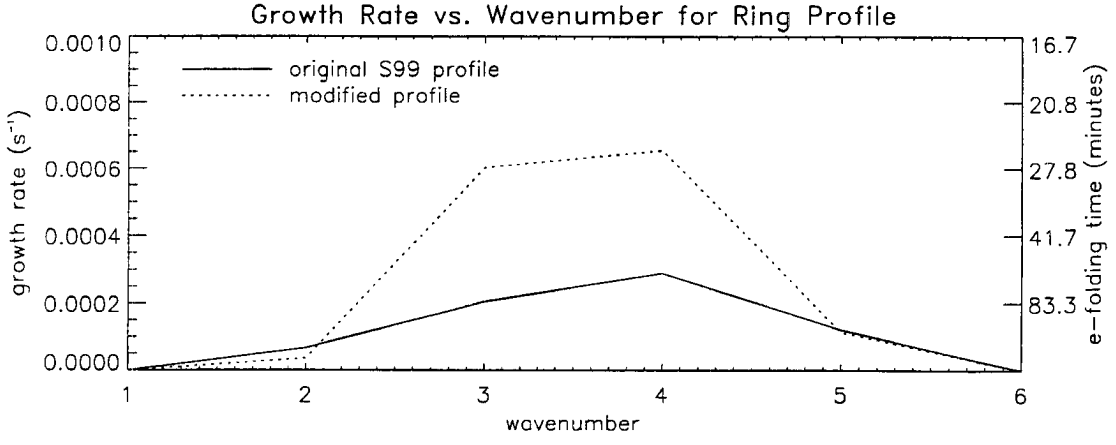

Figure 4.5: Growth rate versus wave number for the modified profile (dotted) and the original S99 profile (solid).

$$\psi'(r,\lambda,t) = \hat{\psi}_n(r)e^{i(n\lambda+\nu t)} \tag{4.4}$$

and

$$\zeta'(r,\lambda,t) = \hat{\zeta}_n(r)e^{i(n\lambda+\nu t)}, \tag{4.5}$$

we then substitute these solutions into the linearized inviscid form of Eq. (2.17). An eigen-analysis of the resultant equation subject to the boundary conditions (2.30) is next performed given the mean vorticity profile $\overline{\zeta}$ specified in (4.1) to determine the eigenfrequencies and eigenstreamfunctions. The imaginary part of the eigenfrequency is a measure of the growth rate for each discrete wavenumber. Fig. 4.5 is a plot of the imaginary part of the eigenfrequencies for wavenumbers 1 through 6 (the growth rates for all other wavenumbers were found to be zero) for the modified ring profile (dotted curve) and for the original S99 profile (solid curve).

According to Fig. 4.5, the most unstable mode for the original S99 profile is $n = 4$. This analysis is in agreement with the results of S99 where a wavenumber 4 feature developed during the initial stages of the vortex evolution (see S99, Fig. 3a) at approximately the same rate predicted by this eigen-analysis.

In the modified profile, while $n = 4$ is clearly the most unstable mode, the growth rate for $n = 3$ is also quite similar. The growth rate is approximately 6.1×10^{-4} s^{-1} for $n = 3$ and approximately 6.6×10^{-4} s^{-1} for $n = 4$. In contrast to S99, the initial stages of the ring vortex evolution are expected to contain a superposition of wavenumbers 3 and 4.

Fig. 4.6 is a plot of the perturbation vorticity field for $n = 3$ and $n = 4$. For each wavenumber, the vorticity anomalies near the elevated ring (indicated by the shaded region) are phase shifted such that they reinforce each other by advecting basic state vorticity. The positive anomalies (solid contours) on the inside (outside) of the ring induce a cyclonic circulation which advects positive basic state vorticity into the positive anomalies on the outside (inside) of the ring, reinforcing the positive perturbation vorticity there. A similar argument holds true for the negative perturbation vorticity anomalies. By this

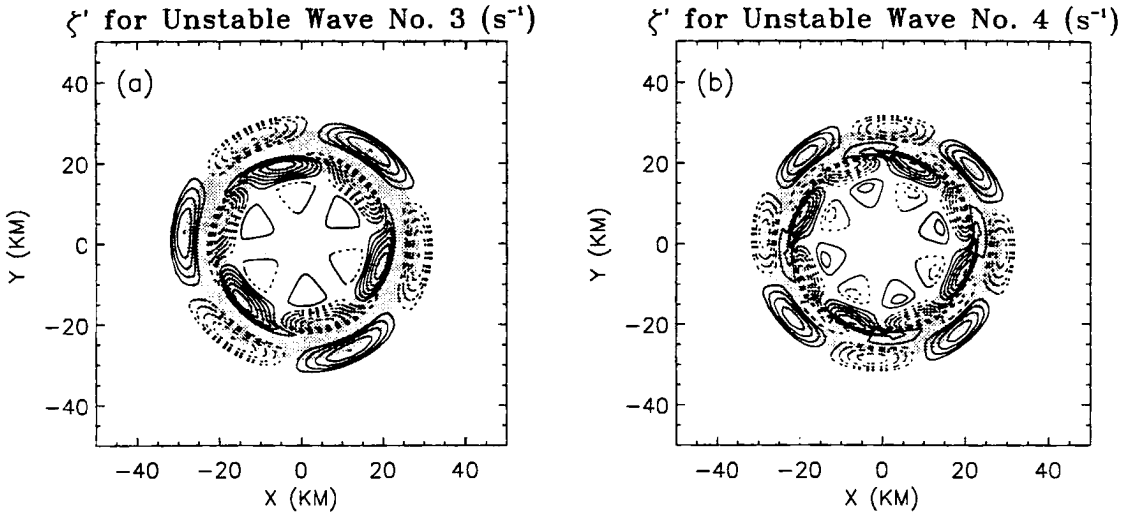

Figure 4.6: Structure of perturbation vorticity field for exponentially unstable modes (a) $n = 3$ and (b) $n = 4$ for the modified profile. Contours begin at -12.0×10^{-8} with increments of 2.0×10^{-8}.

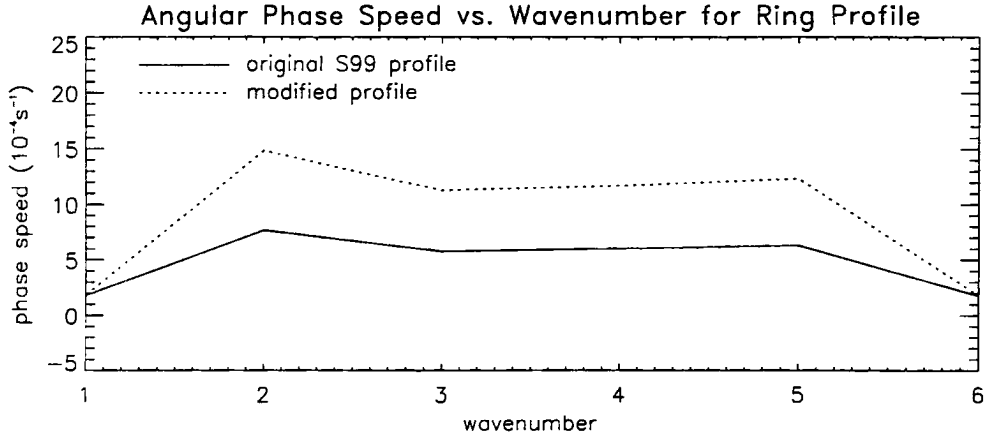

Figure 4.7: Angular phase speed versus wave number for the modified profile (dotted) and the original S99 profile (solid).

mechanism, the asymmetric vorticity fields for $n = 3$ and $n = 4$ feed off the basic state flow and grow.

Fig. 4.7 is a plot of the angular phase speeds ($c_{p\lambda} = Re[\nu]/n$) determined from the eigen-analysis. It shows that $n = 2$ has the fastest angular velocity, with $n = 3$, 4, and 5 having comparable values in both the modified and original S99 profiles. The phase speeds for the modified profile are also substantially faster (by about a factor of 2) than those for the original S99 profile for all wavenumbers with non-zero growth-rates (i.e., $n\epsilon\{2, 3, 4, 5\}$). We observe that the maximum phase speed for the modified profile is approximately 1.5×10^{-3} s^{-1} while the maximum angular rotation rate throughout the vortex (Fig. 4.3b) is approximately 1.9×10^{-3} s^{-1}. This means that the unstable waves retrograde relative to the fastest rotating part of the fluid, a feature already anticipated by vortex Rossby wave theory.

Based on this analysis, we expect to see a faster route to vorticity mixing in the modified case as compared to S99.

4.2.3 Perturbation

The basic state circular flow is perturbed with the following perturbation vorticity :

$$\zeta'(r,\phi,t=0) = \hat{\zeta}\sum_{m=1}^{8}\cos(m\phi)\begin{cases} 0, & 0 \le r \le r_1 - d_1 \\ S((r_1+d_1+1-r)/2d_1), & r_1 - d_1 \le r \le r_1 + d_1 \\ 1, & r_1 + d_1 \le r \le r_2 - d_2 \\ S((r-r_2+d_2)/2d_2), & r_2 - d_2 \le r \le r_2 + d_2 \\ 0, & r_2 + d_2 \le r \le \infty. \end{cases} \tag{4.6}$$

In our case, $\hat{\zeta} = 0.01\ \overline{\zeta}_{\max} = 7.0 \times 10^{-5}$ s^{-1}. Summing over all 8 wavenumbers leads to a maximum perturbation vorticity of $\zeta'_{\max} = 0.08\ \overline{\zeta}_{\max} = 5.6 \times 10^{-4}$ s^{-1} centered at $\lambda = 0$ and $r = 50$ km (see Fig. 4.8). Similar to the perturbation in the monopole experiment, this perturbation is intended to simulate a convective disturbance near the RMW, but in this case the perturbation is smaller in amplitude (8% of $\overline{\zeta}_{\max}$ as opposed to 50% of $\overline{\zeta}_{\max}$ in the monopole experiments).

Plots of (4.6) and the total field of ζ for a 100 km $\times$ 100 km subset of the entire domain are given by Figs. 4.8b and c, respectively. Note the maximum of ζ' just inside the RMW.

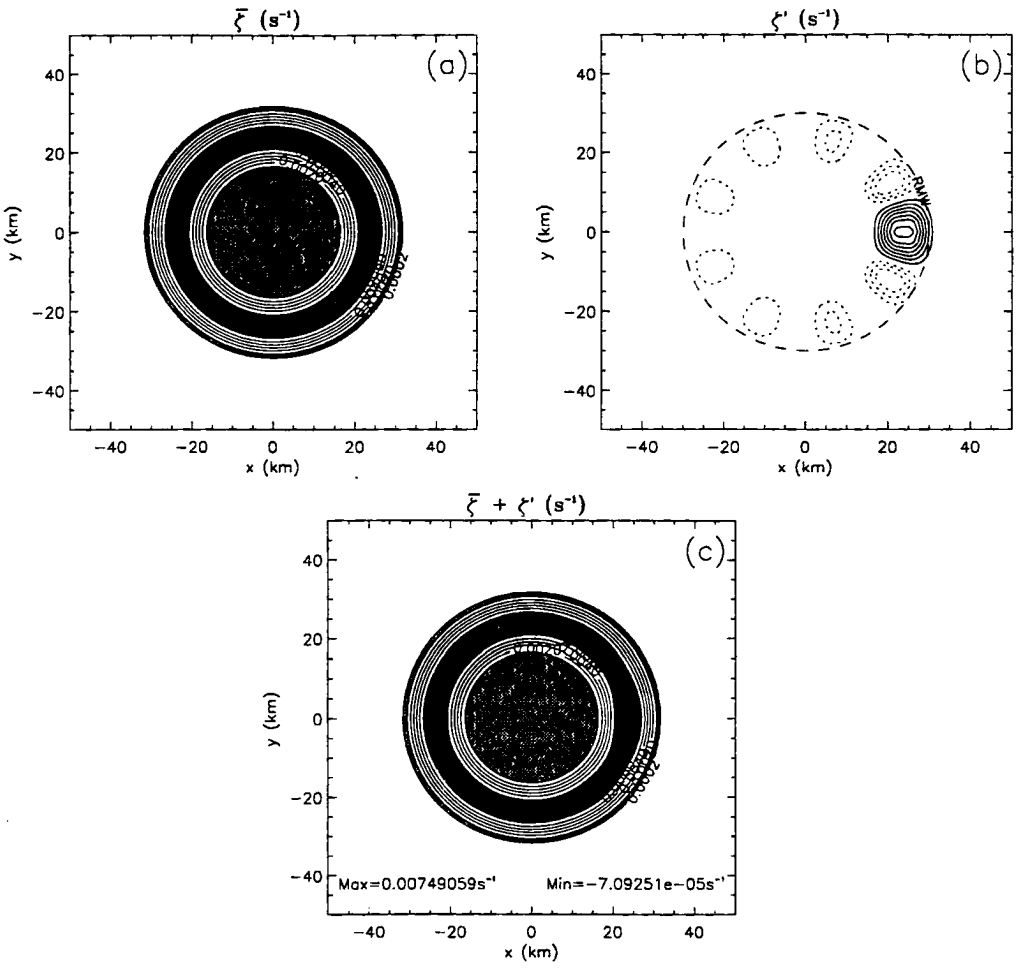

Figure 4.8: Initial plots of (a) basic state, (b) perturbation and (c) total relative vorticity as functions of x and y over a 100 km $\times$ 100 km subset of the entire domain. For plots (a) and (c), the lowest contour level is 2.0×10^{-4} s^{-1} with the remaining contour levels beginning at 1.0×10^{-3} s^{-1} in increments of 1.0×10^{-3} s^{-1}. In plot (b), the solid contours begin at 7.5×10^{-5} s^{-1} and are incremented by 7.5×10^{-5} s^{-1}, while the dotted contours begin at -4.0×10^{-5} s^{-1} and are decremented by 4.0×10^{-5} s^{-1}. Grey indicates $2.0 \times 10^{-4} s^{-1} \leq \zeta \leq 1.0 \times 10^{-3}$ s^{-1}, and black indicates $\zeta \geq 6.0 \times 10^{-3}$ s^{-1}. $\overline{\zeta}_{\max} = 7.0 \times 10^{-3}$ s^{-1} and $\zeta'_{\max} = 5.6 \times 10^{-4}$ s^{-1}.

4.3 Model Setup

The following table summarizes the numerical parameters used in the ring experiment for the SP and SS models:

	SP	**SS**
Viscosity (ν)	100 m^2s^{-1}	100 m^2s^{-1}
No. gridpoints	x: 900, y: 900	r: 640
Gridspacing	$dx = dy = 0.5$ km	$dr = 0.5$ km
No. of modes	x: 300, y: 300	λ: 32
Timestep	4 s	2 s
Degrees of Freedom	$(900)^2 = 810,000$	(640)(64)=40,960

Table 4.1: Numerical parameters used in the SP and SS models for the ring experiments.

Note from Table 4.1 that the SP model is run with 300 modes in x and y, while the SS model is run with only 32 azimuthal modes. Also note that the timestep for the SP model is twice that for the SS model. Through the course of this study, we empirically determined that the CFL stability condition (Courant-Friedrichs-Lewy; see Press, et al., 1992 for details) for the SP model requires a time step on the order of one-half the advective time scale, $(1/2)\Delta/\overline{v}_{\tan,\max}$ where $v_{\tan,\max}$ is the maximum tangential wind speed and Δ is the grid spacing. For the SS model with 32 azimuthal modes, the stability boundary was found to be on the order of one-fourth the advective time scale, $(1/4)\Delta/\overline{v}_{\tan,\max}$. This yields Δt's of approximately 4 s and 2 s for the SP and SS models, respectively.

As in Section 3.3, a more realistic estimate of the resolution for the SP model is the wavelength of the smallest resolvable Fourier mode which is approximately 1.5 km (three times the grid spacing between collocation points; S99, Sect. 3).

For the SS model, a more realistic estimate of the azimuthal resolution is the wavelength of the smallest resolvable Fourier mode at the RMW. This is approximately 5.9 km for the ring experiment. In the radial direction, we assume the wavelength of the smallest resolvable mode will be equal to 4 times the grid spacing. This yields an effective radial resolution of 2 km for the SS model.

4.4 Expected Results

Since we initialize our models in a somewhat similar fashion to S99, we expect to see a somewhat similar evolution. That is, we expect unstable vortex Rossby waves to develop in the flow and break the ring into vortical eddies. From Sect. 4.2.2 these eddies should initially take on a superposed pattern of wavenumbers 3 and 4. We expect the eddies to mix high vorticity inward and low and high vorticity outward via an active enstrophy cascade. And we expect that the endstate will be an approximate monopole similar to the endstate achieved in S99.

4.5 Results

4.5.1 Observed Growth Rates

Here we examine the actual growth rates observed in the simulation as a function of wavenumber and compare them to the growth rates predicted in Sect. 4.2.2. Since our eigen-analysis was for the linearized form of Eq. (2.17), we compare the growth rates that occur in the simulation while the vortex evolution is linear in nature. From Figs. 4.11 and 4.12 we observe that the evolution is still linear up to 1 h into the simulation (panel b in both figures) but becomes nonlinear somewhat after this time (as evident by the stretched and folded contours at $t = 1.5$ h). As a result, we compare observed growth rates at $t =$ 1 h to see if they agree with the exponential growth rates predicted in Fig. 4.5.

Figure 4.9 shows the time evolution of the maximum Fourier amplitude $\hat{\zeta}_{n,\max}$ through $t = 4$ h for wavenumbers 1 through 5. Figure 4.10 shows the evolution of the observed growth rates $(1/\hat{\zeta}_{n,\max})d/dt(\hat{\zeta}_{n,\max})$ from $t = 0.25$ h to $t = 1.5$ h. The two dashed vertical lines in Fig. 4.10 indicate the interval in which the growth rates are approximately constant, a distinguishing attribute of exponential growth. We only examine the growth rates for $n = 3$ and $n = 4$ since these modes have the highest growth rates in this interval and were predicted to be the largest in Sect. 4.2.2. For $n = 4$ the observed growth rate is approximately 6.4×10^{-4} s^{-1}, while for $n = 3$, the observed growth rate is approximately 6.0×10^{-4} s^{-1}. These values are in good agreement with the values in Fig. 4.5 where we

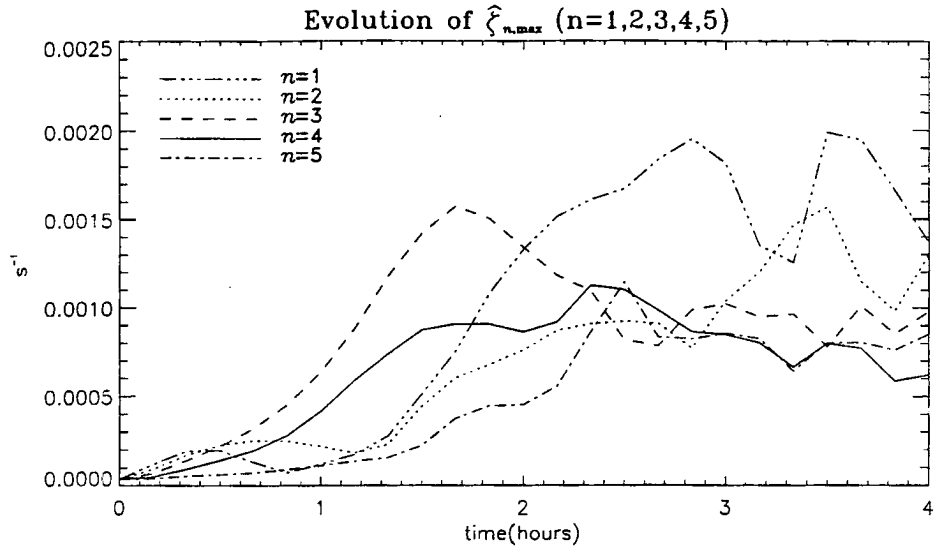

Figure 4.9: Evolution of the maximum of the eigenfunction $\hat{\zeta}_{n,\max}$ for wavenumbers 1 through 5 from $t = 0$ to $t = 4$ h.

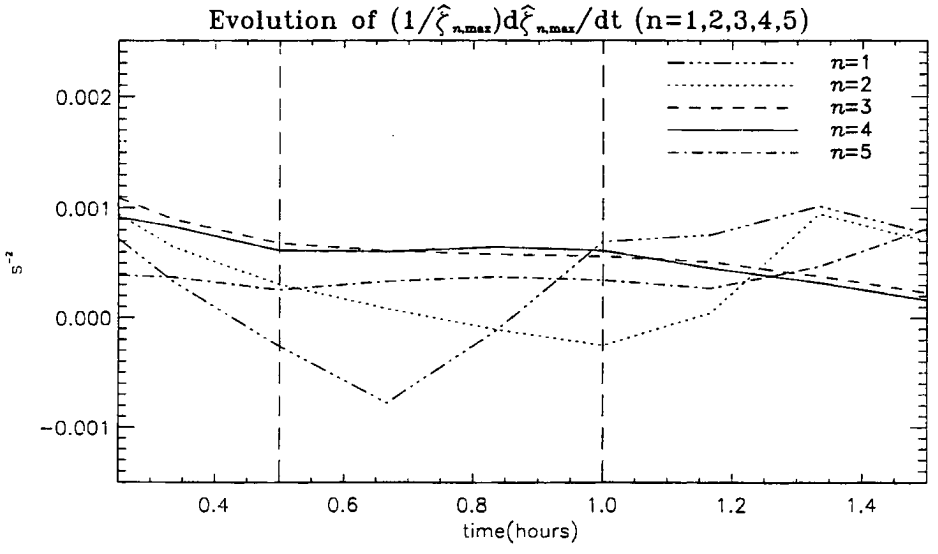

Figure 4.10: Evolution of the growth rates $(1/\hat{\zeta}_{n,\max})d\hat{\zeta}_{n,\max}/dt$ for wavenumbers 1 through 5 from $t = 0.25$ to $t = 1.5$ h.

predicted growth rate of approximately 6.6×10^{-4} s^{-1} and 6.1×10^{-4} s^{-1} for $n = 4$ and $n = 3$, respectively.

4.5.2 Vortex Evolution

The following figures show the results of this set of experiments. The SP model results are shown first (Fig. 4.11) followed by the SS model results (Fig. 4.12).

We first examine the evolution of the total field plots of vorticity given by Figs. 4.11 and 4.12. Notice the striking similarity between the two models. Both models initially develop an instability pattern (a superposition of wavenumber 3 and 4) a short time into the run. This instability eventually develops into vortical eddies which, in turn, initiate the vorticity redistribution into an approximate monopole.

By comparing the two figures, we get a sense that the SS model is performing very well at capturing the essence of the vortex evolution. The main discrepancy between the models shows up in the form of numerical dispersion errors that are obvious beginning with Fig. 4.12d. These errors are the result of the finite difference approximations in the radial coordinate. Unlike the continuous case for a simple wave equation where all the waves have the same phase speed, the finite difference representation of derivatives results in a spectrum of waves that have slightly different phase speeds. These waves are therefore dispersive and lead to "dispersion errors." This problem can be minimized with a more accurate finite differencing scheme (e.g., fourth order versus second order) or a finer radial grid mesh.

A second numerical error is observed by examining the normalized maximum values (N_max) located in the upper-left corner of all panels. It is evident that the SS model tends to increase (overshoot) the maximum value of the vorticity while the SP model generally decreases this maximum over the course of the run with no noticeable overshoot. This error is partly due to the finite difference approximation of the radial derivatives and also to the severe azimuthal truncation for small-scale vorticity structures that develop in the azimuthal direction in a flow with extensive mixing (Gibbs phenomenon). As with the previously observed dispersion errors, this error can be reduced by employing a more accurate differencing scheme, a finer mesh grid, or increased azimuthal resolution.

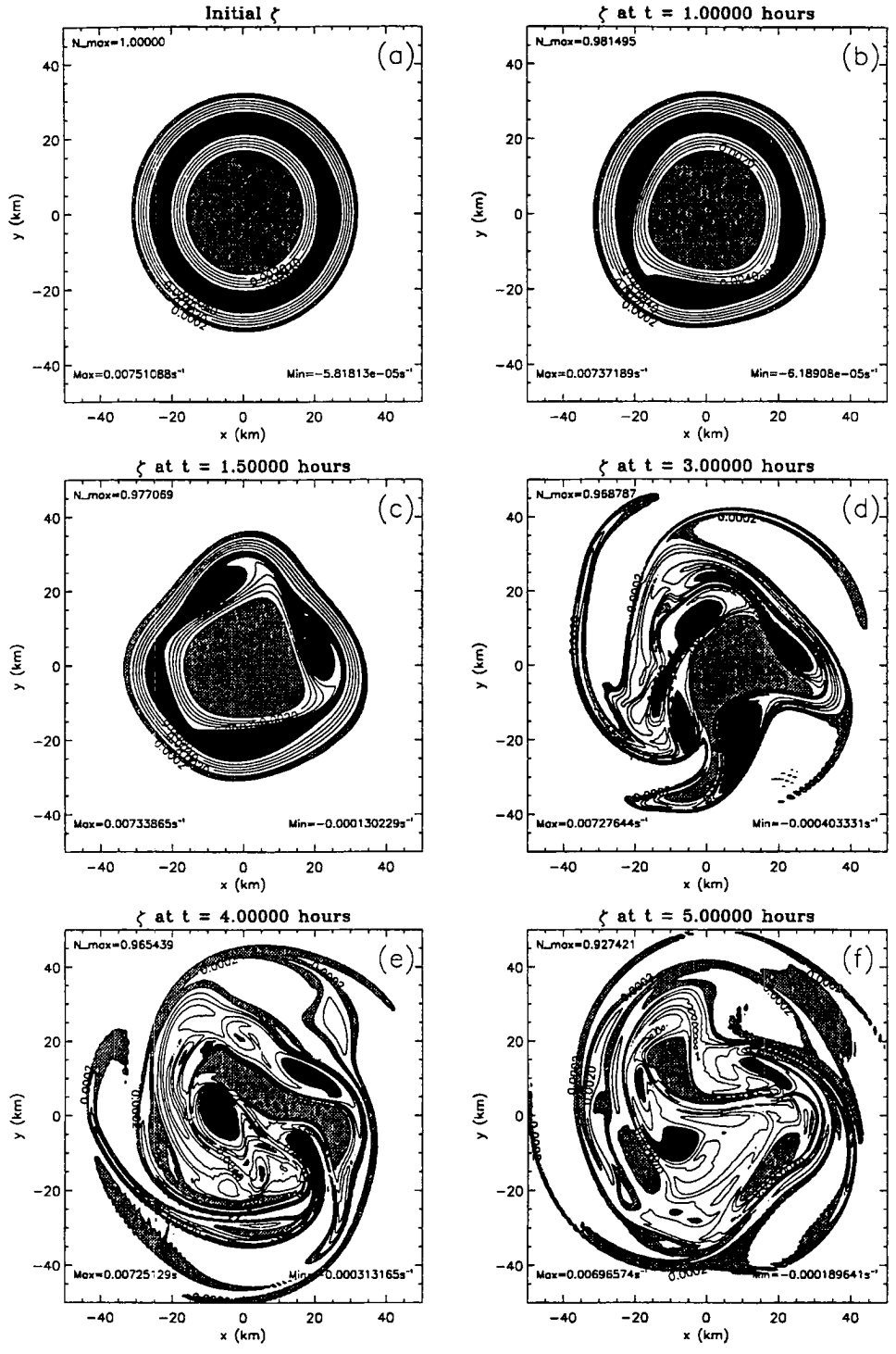

Figure 4.11: SP model vorticity evolution for the ring experiment from $t = 0$ to 5 h. In each panel, a 100 km $\times$ 100 km subset of the entire domain is plotted. The lowest contour level is 2.0×10^{-4} s^{-1} with the remaining contour levels beginning at 1.0×10^{-3} s^{-1} in increments of 1.0×10^{-3} s^{-1}. Grey indicates 2.0×10^{-4} s^{-1} $\leq \zeta \leq 1.0 \times 10^{-3}$ s^{-1}, and black indicates $\zeta \geq 6.0 \times 10^{-3}$ s^{-1}.

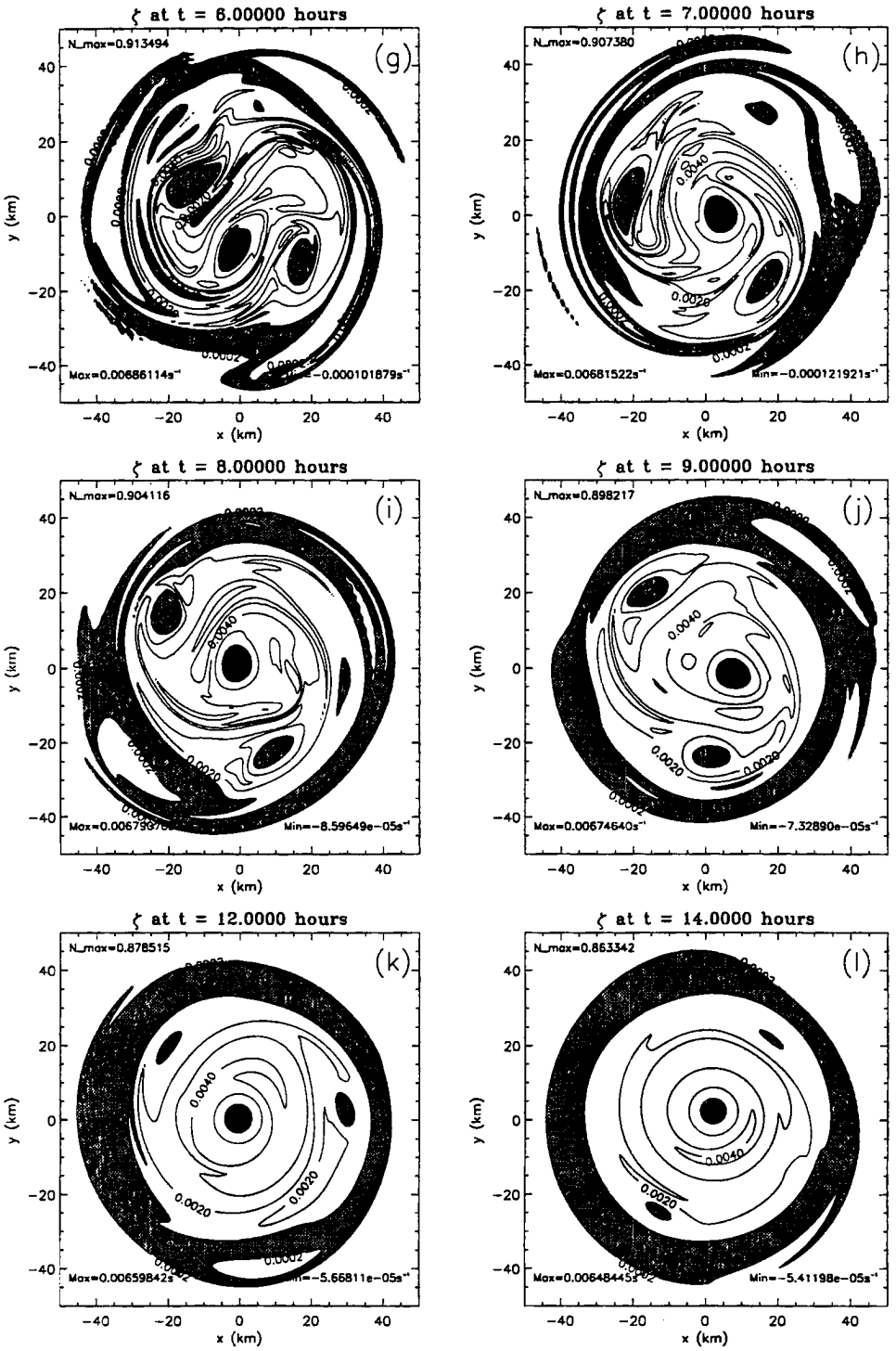

Figure 4.11: *continued* Vorticity from $t = 6$ to 14 h.

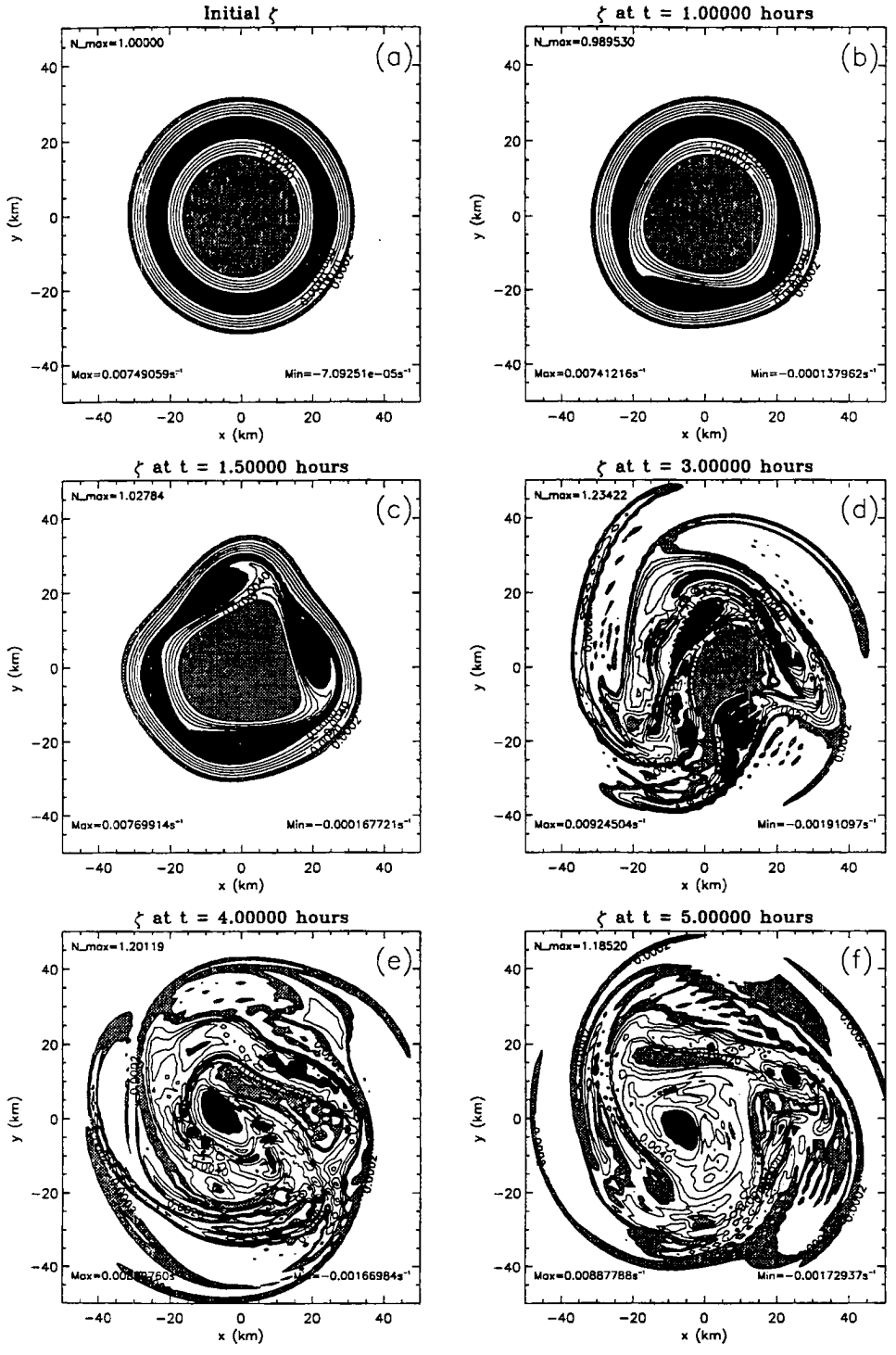

Figure 4.12: SS model vorticity evolution for the ring experiment from $t = 0$ to 5 h. In each panel, a 100 km × 100 km subset of the entire domain is plotted. The lowest contour level is 2.0×10^{-4} s^{-1} with the remaining contour levels beginning at 1.0×10^{-3} s^{-1} in increments of 1.0×10^{-3} s^{-1}. Grey indicates 2.0×10^{-4} s^{-1} $\leq \zeta \leq 1.0 \times 10^{-3}$ s^{-1}, and black indicates $\zeta \geq 6.0 \times 10^{-3}$ s^{-1}.

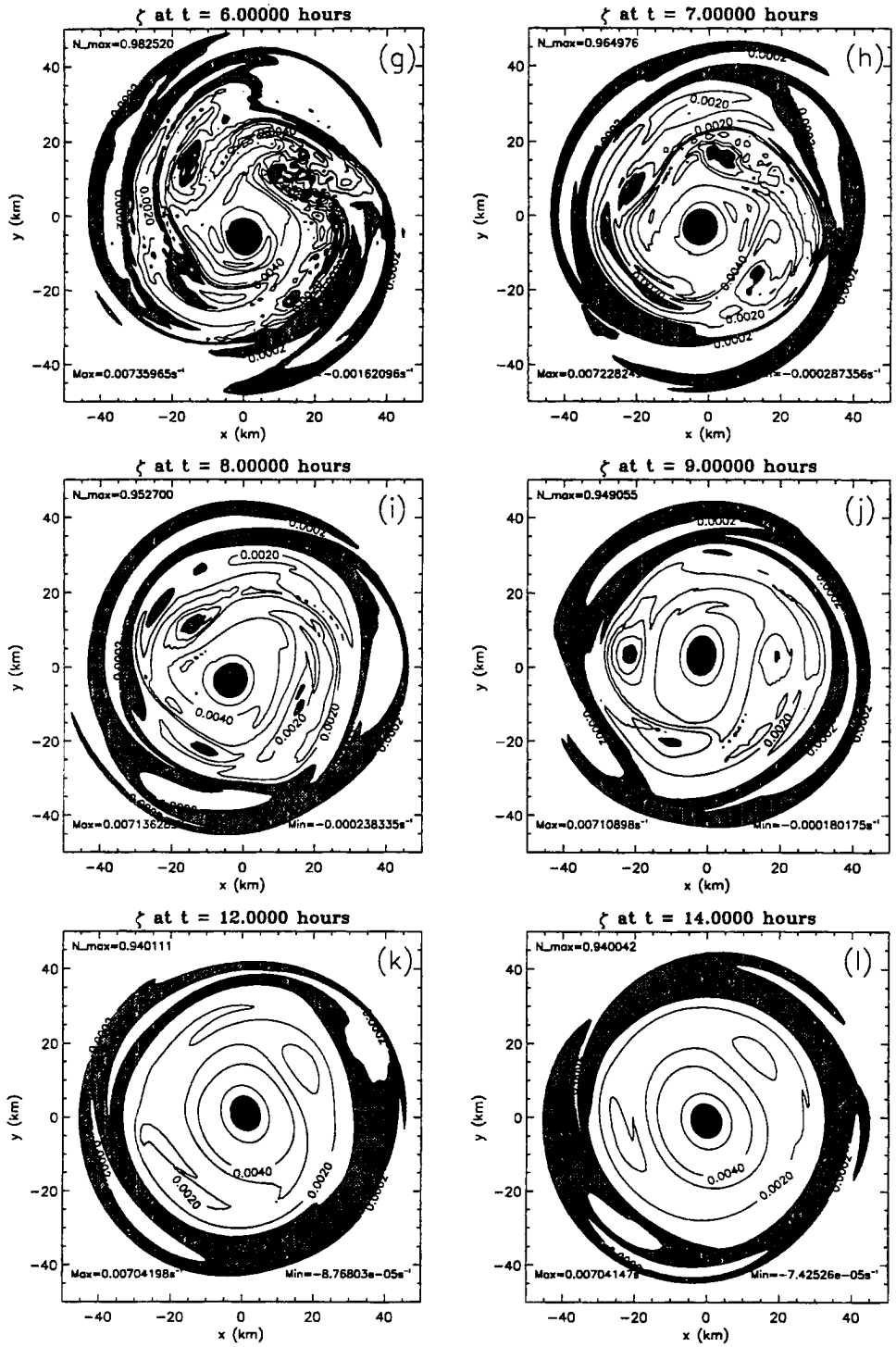

Figure 4.12: *continued* Vorticity from $t = 6$ to 14 h.

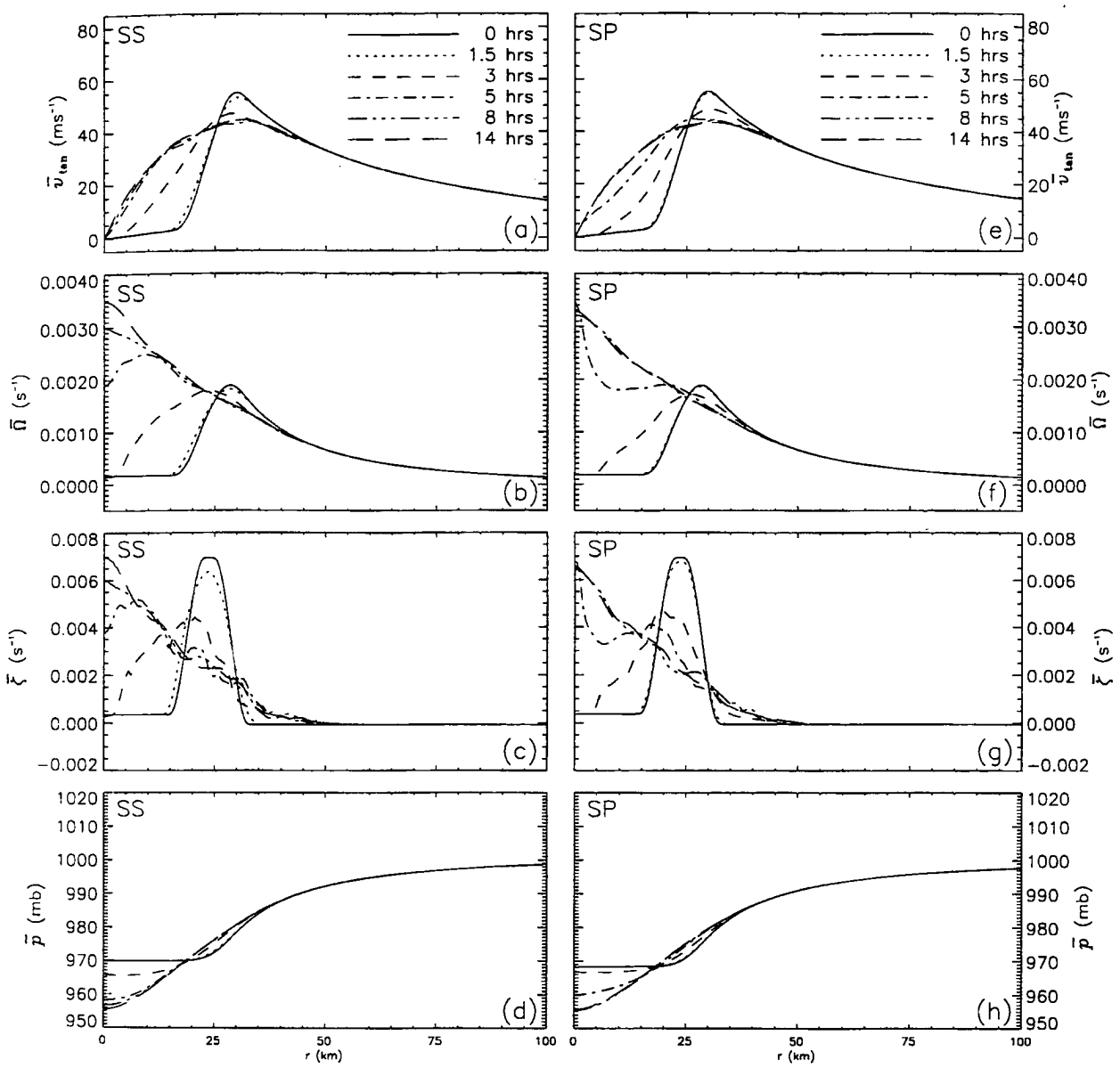

Figure 4.13: Evolution of the azimuthal mean tangential wind ($\overline{v}_{\tan}$), angular rotation rate ($\overline{\Omega}$), vorticity ($\overline{\zeta}$), and pressure ($\overline{p}$) for both models at $t = 0$ h (solid), 1.5 h (dotted), 3 h (dashed), 5 h (dash-dot), 8 h (dash-dot-dot-dot), and 14 h (long dashes). Panels (a) through (d) are for the SS model, and (e) through (h) are for the SP model.

Changes in Mean Quantities

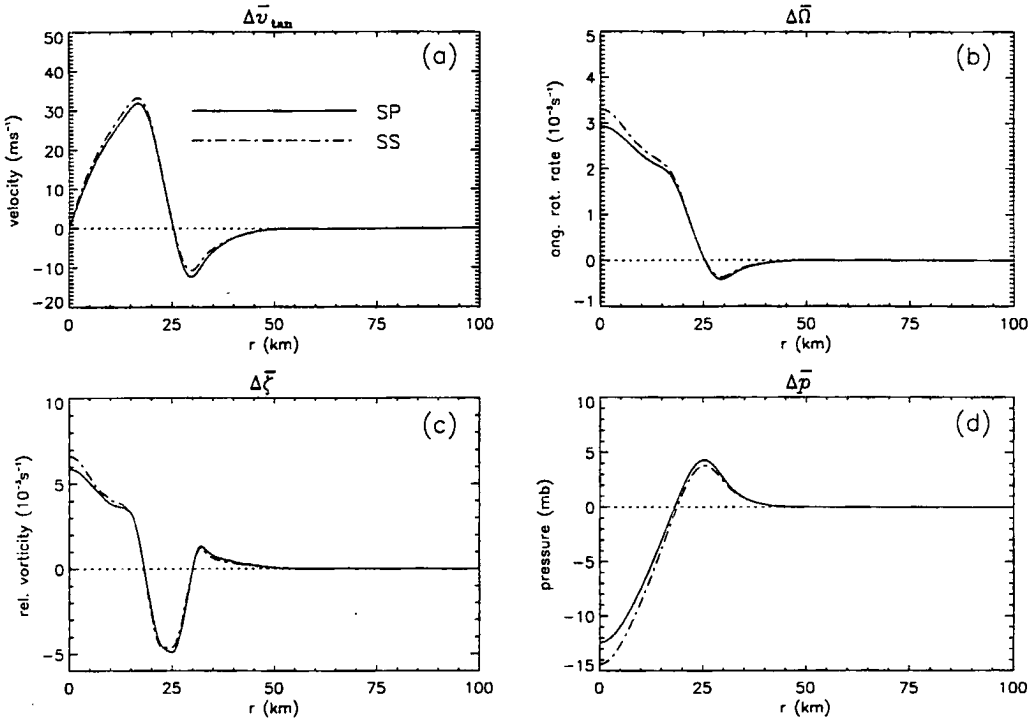

Figure 4.14: Changes in the azimuthal mean (a) tangential wind ($\overline{v}_{\tan}$), (b) angular rotation rate ($\overline{\Omega}$), (c) vorticity ($\overline{\zeta}$), and (d) pressure ($\overline{p}$) over the course of the run for the SP model (solid) and SS model (dash-dot). The units for the $\overline{\Omega}$ and the $\overline{\zeta}$ plots are 10^{-3} s^{-1}.

We next examine changes in the mean quantities that are a result of the lifecycle of the instability (Fig. 4.14). The plots show that nearly identical results are obtained with each model. The SS model yields a final vorticity maximum that is 94% of the initial maximum, while the SP model yields a final vorticity maximum that is 84.3% of the initial maximum. The corresponding pressure deepening is slightly stronger in the SS model than the SP model. Nevertheless, the overall nature of the changes (i.e., location and general strength) are very similar. This is further illustrated in the plots of the evolving radial profiles of these quantities shown in Fig. 4.13. With as little as 32 azimuthal modes (compared to the 300 $\times$ 300 modes required for the SP model), the SS model produces nearly the same endstate as the SP model.

Domain-Integrated Quantities

As in Chapter 3, we examine area-integrated quantities (Fig. 4.15). The SS model appears to more nearly conserve energy, enstrophy, and angular momentum than does the SP model, which was also observed in the monopole case. Also note that the plots of palinstrophy show a slight difference between the models in terms of the maximum values obtained. These discrepancies notwithstanding, we observe similar results. As in the previous chapter, this further suggests that the SS scheme is adequately representing the dynamics of the vortex evolution.

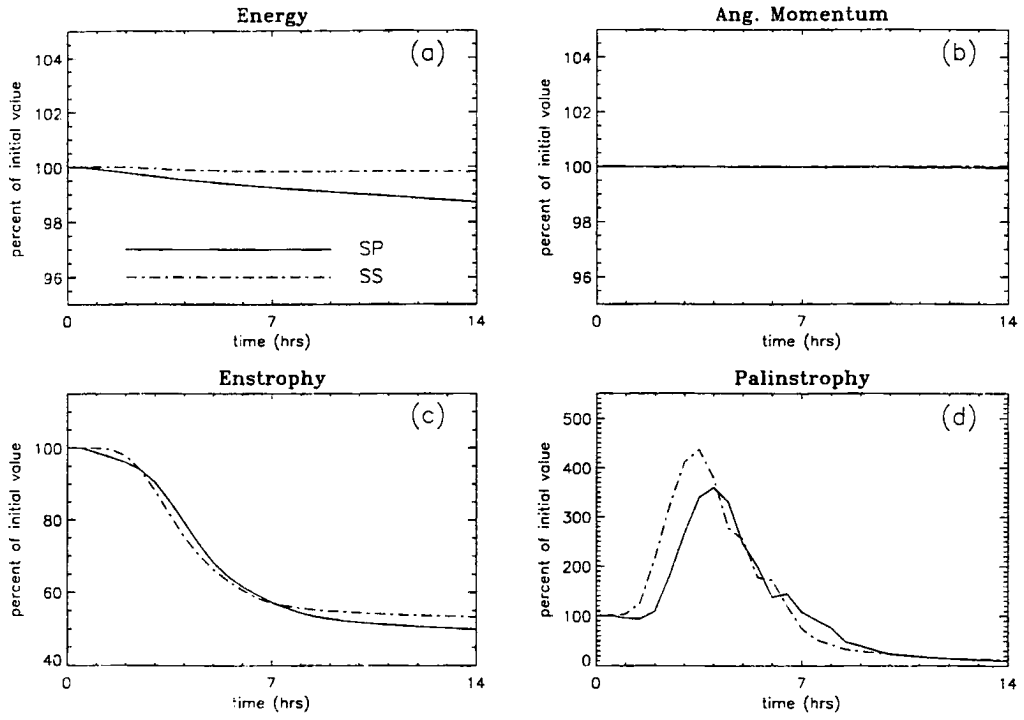

Figure 4.15: Time evolution of integrated (a) total energy ($E = \int\int \frac{1}{2} \nabla \psi \cdot \nabla \psi \, dA$), (b) angular momentum ($AM = \int\int r^2 \zeta \, dA$), (c) enstrophy ($V = \int\int \frac{1}{2} \zeta^2 \, dA$), and (d) palinstrophy ($P = \int\int \frac{1}{2} \nabla \zeta \cdot \nabla \zeta \, dA$) over the course of the run for the SP model (solid) and the SS model (dash-dot). Values are normalized based on the initial value. Note the scale changes from (b) to (c) and (c) to (d).

4.5.3 Timing Data

Finally, we examine computer time requirements for each model to run to completion for the unstable ring configuration. Table 4.2 shows that the SS model formulation was

MODEL	RUN TIME (CPU)
SP	14,625 min (~10 days)
SS	5,764 min (~4 days)

Table 4.2: Timing data for the two ring runs based on the amount of CPU time required for each model to run to completion for a 14 h vortex simulation.

able to obtain the endstate in less than half the time required by the SP model for the numerical parameters chosen.

4.5.4 Comparison With Some of the Principle Results of S99

The initial vortex for this set of experiments was a modification of the S99 vortex in which the RMW was reduced from 60 km to 30 km and the maximum vorticity was nearly doubled. A more realistic hurricane-like vortex was thus obtained with stronger initial vorticity gradients and higher instability growth rates than S99. As a result and perhaps most importantly, the duration of the mixing was reduced from approximately 36 h to approximately 14 h, a more realistic estimate of the timescale for vorticity mixing in hurricane-like vortices.

It is also interesting to note the low vorticity lobes that circle the vortex center beginning at approximately $t = 7$ h (panel h in Figs. 4.11 and 4.12). These two regions orbit the center for the remaining 7 h of the evolution with no apparent effect on the shape of the central vorticity region. A similar feature was noted in S99 expect that the core of the low-vorticity region was ejected en masse from the center without any breakup.

A further difference between S99 and the present simulation regards the change in the central pressure of the vortex. A deepening of approximately 8 mb is evident in Fig. 9c of S99 while a 12 mb pressure drop is observed in Fig. 4.14, a 50% change in the pressure deficit.

These differences are ultimately attributable to the higher wind shear and the stronger vorticity gradient on the edges of the ring in the modified vortex. Additionally, from the standpoint of the linear instability theory of Section 4.2.2, the maximum growth rates and angular phase speeds for the most unstable modes of the modified vortex are roughly twice as large as for the S99 vortex, causing the onset of mixing to occur sooner.

We thus believe the evolution presented, although still highly idealized, is a bit more representative of the vorticity mixing processes in the eye region of real-world hurricanes that are weakly forced and satisfy the sufficient condition for barotropic instability.

4.6 Ring Vortex Conclusions

For the ring experiment, we have shown that the SS model provides reasonably accurate results with fewer modes and in less time than the SP model for the numerical parameters chosen. In this simulation (and others not shown), the SS model produced notable numerical dispersion and overshoot errors in the vorticity field. Nevertheless, the gross nature of the evolving vorticity field and final endstates still approximately matched the SP simulation.

Chapter 5

CONCLUSIONS

In this study we have examined a semispectral (SS) numerical model for its effectiveness in simulating the dynamics of vortex flows, particularly hurricanes. The term "semispectral" implies a model formulated in a cylindrical coordinate system and incorporating both finite difference and spectral methods. Here, we have limited the focus of this study to determining how this hybrid method performs relative to "pure" methods (a finite difference (FD) model and a spectral (SP) model) in terms of computational accuracy and speed. We proceeded by simulating two classes of problems: (1) the redistribution of vorticity anomalies within a parent "master" vortex whose vorticity profile decreases monotonically with radius and (2) the vorticity mixing processes akin to what is observed near the eye region of mature hurricanes. We then analyzed the output and timing data and were able to draw conclusions on the effectiveness of the SS scheme in simulating these two types of vortices, relative to the FD and SP schemes.

In the first set of experiments, we simulated the axisymmetrization of nearby vorticity anomalies on a basic state "master" vortex whose vorticity decreases monotonically with radius (as in ME). We found that the SS model performed very well. It was able to generate virtually identical results to both the FD and SP schemes on nearly all scales. The evolution of the vortex, the changes in the mean quantities ($\Delta\overline{v}_{\tan}$, $\Delta\overline{\Omega}$, $\Delta\overline{\zeta}$, and $\Delta\overline{p}$), and the time evolution of area-integrated quantities (kinetic energy, angular momentum, and enstrophy) calculated by the SS model were virtually identical to those calculated by the FD and SP models. Furthermore, the amount of computer time required for the SS model to run to completion was less than half that required of the SP model and nearly one-tenth that of the FD model for the numerical parameters chosen. Thus, when

simulating tropical depression-like vortices with a monopolar vorticity structure, the SS scheme generally provides highly accurate results in less time required by either the FD or SP numerical schemes.

Our second set of experiments provided a more stringent test of the SS model by simulating the barotropic instability and breakdown of a mature hurricane-like vortex possessing an elevated vorticity maximum at a finite radius from the vortex center. This set of experiments is motivated by the recent work of S99 who employed the SP model to analyze the lifecycle of such unstable ring profiles. Since the baseline performance of each model and the relative performance characteristics between models had already been established in the perturbed monopole experiment, only the SP model was employed as a control.

This second set of experiments showed that the SS model was again able to reproduce the overall evolution of the vortex as compared to the SP model. However, some problems with numerical dispersion and overshoot of the maximum vorticity in the fluid were observed. Barring these local errors, the SS model adequately simulated the essence of the dynamics including locations of relative maxima and minima well into the nonlinear mixing phase and achieved these results in less than half the time required by the SP model for the numerical parameters chosen. Furthermore, and perhaps most importantly from the standpoint of predicting mean flow structure and intensity changes, the SS model predicted the final endstate to a high degree of accuracy.

It is important to note that the results obtained in the second set of experiments are considered a bit more realistic for mature hurricanes than the S99 results. In our case, the vortex was smaller, the elevated value of vorticity was greater, and the growth rates for the most unstable modes were larger. This resulted in a mixing duration of 14 h with a pressure deepening of 12 mb. The simulated mixing time is believed a more realistic estimate of the mixing timescale in mature hurricanes.

Some of the questions posed in Chapter 1 can now be answered. The SS scheme, taking advantage of the near-circular symmetry of the hurricane and using Fourier modes in the azimuthal direction and finite difference approximations in the radial direction, has

been shown to be a useful research tool for examining the near-core vortex dynamics of tropical cyclone-like vortices. Particular instances in which this method may be desirable over other methods are: (1) when quick results are needed, (2) when computer time is limited, and (3) to perform many different runs with varying initial conditions (i.e., sensitivity tests and ensemble forecasts). The SS method is especially advantageous for modeling processes which generate low azimuthal wavenumber vortex Rossby waves and when the structure of the endstate is the main goal of the numerical experiment. In summary, the SS model is a natural and effective tool that should be exploited by researchers in studying the near-core dynamics of hurricane-type vortices.

REFERENCES

Arakawa, A, 1966: Computational design for long-term numerical integration of the equations of fluid motion: Two-dimensional incompressible flow. Part I. *J. Comput. Phys.*, **1**, 119–143.

Charney, J. G., Fjørtoft, R., and J. von Neumann, 1950: Numerical integration of the barotropic vorticity equation. *Tellus*, **2**, 237–254.

Edwards, J. P., 1994: Barotropic Instability in the Inner core of Tropical Cyclones. *Colorado State University*, Atmospheric Science Paper No. 552.

Eliassen, A., and M. Lystad, 1977: The Ekman layer of a circular vortex. A numerical and theoretical study. *Geophys. Norv.*, **31**, 1–16.

Fjørtoft, R., 1950: Application of integral theorems in deriving criteria of stability for laminar flows and for the baroclinic circular vortex. *Geofys. Publ.*, **17**, No 6, 52pp.

Gent, P. R., and J. C. McWilliams, 1986: The instability of barotropic circular vortices. *Geophys. Astrophys. Fluid Dyn.*, **35**, 209–233.

Gray, W. M., 1998: The formation of tropical cyclones. *Meteorol. Atmos. Phys.*, **67**, 37–69.

Guinn, T. A., and W. H. Schubert, 1993: Hurricane spiral bands. *J. Atmos. Sci.*, **50**, 3380–3403.

Haltiner G. J., and R. T. Williams, 1980: *Numerical Prediction and Dynamic Meteorology*. 2nd Ed. John Wiley and Sons, Inc. 477 pp.

Montgomery, M. T., and J. E. Enagonio, 1998: Tropical cyclogenesis via convectively forced vortex Rossby waves in a three-dimensional quasigeostrophic model. *J. Atmos. Sci.*, **55**, 3176–3207.

Montgomery, M. T., and R. J. Kallenbach, 1997: A theory for vortex Rossby waves and its application to spiral bands and intensity changes in hurricanes. *Quart. J. Roy. Meteor. Soc.*, **123**, 435–465.

Montgomery, M. T., Möller, J. D., and Christopher T. Nicklas, 1999: Linear and nonlinear vortex motion in an asymmetric balance shallow water model. *J. Atmos. Sci.*, **56**, 749–768.

Press, W. H., Teukolsky, S. A., Vettering, W. T., and B. P. Flannery, 1992 *Numerical Recipes in FORTRAN. The Art of Scientific Computation.* 2nd Ed. Cambridge University Press, 963 pp.

Rayleigh, Lord, 1880: On the stability or instability, of certain fluid motions. *Scientific Papers, Vol. 3*, **56**, 1197–1223.

Schubert, W. H., Montgomery M. T., Taft, R. K., Guinn, T. A., Fulton, S. R., Kossin, J. P., and J. P. Edwards, 1999: Polygonal eyewalls, asymmetric eye contraction, and potential vorticity mixing in hurricanes. *J. Atmos. Sci.*, **56**, 1197–1223.

Swarztrauber, P., and R. A. Sweet, 1975: Efficient FORTRAN subprograms for the solution of elliptic partial differential equations. NCAR technical note TN/IA-109. 139 pp.

Willoughby, H. E., 1988: Linear motion of a shallow water, barotropic vortex. *J. Atmos. Sci.*, **45**, 1906–1928.

Willoughby, H. E., 1990: Linear normal modes of a moving, shallow-water barotropic vortex. *J. Atmos. Sci.*, **47**, 2141–2148.

Willoughby, H. E., 1992: Linear motion of a shallow-water barotropic vortex as an initial value problem. *J. Atmos. Sci.*, **49**, 2015–2031.

Willoughby, H. E., 1994: Nonlinear motion of a shallow water barotropic vortex. *J. Atmos. Sci.*, **51**, 3722–3744.

Willoughby, H. E., 1995: Normal-mode initialization barotropic vortex motion models. *J. Atmos. Sci.*, **52**, 4501–4514.